SUPPORTING INFORMATION FOR

Tuning intermediate adsorption in structurally ordered substituted $PdCu_3$ intermetallic nanoparticles for enhanced ethanol oxidation reaction

Rajkumar Jana,[a] Ayan Datta,[a,*], Sudip Malik [b,*]

[a] School of Chemical Sciences, Indian Association for the Cultivation of Science, Kolkata-700032, India
E-mail: spad@iacs.res.in

[b] School of Applied & Interdisciplinary Sciences, Indian Association for the Cultivation of Science, Kolkata-700032, India
E-mail: psusm2@iacs.res.in

Experimental section:

Materials: Palladium acetylacetonate ($Pd(acac)_2$) (99%), copper acetylacetonate ($Cu(acac)_2$) (≥99.9%), oleylamine (technical grade, 70%), hexdecyltrimethylammonium bromide (CTAB) and nafion binder (5 wt% in a mixture of lower aliphatic alcohols and water) were purchased from Sigma-Aldrich. All the chemicals were used as purchased without further purification. Millipore water of conductivity 18.2 MΩcm was used for synthesis and all electrochemical studies.

Synthesis: In a typical solvothermal preparation, 0.1 mmol $Pd(acac)_2$, 0.3 mmol $Cu(acac)_2$ and 75 mg of CTAB were mixed together in 18 ml oleylamine in a 23 ml Teflon-lined autoclave. The solution mixture was vigorously stirred for 30 minutes and autoclave was kept in oven at 180°C for 24 hrs. The resulting product was washed repeatedly with 1:1 mixture of ethanol and hexane for several times and re-dispersed the obtained product in hexane.

Characterization: Powder XRD (PXRD) measurements for all the synthesized NPs were done at room temperature with a X'Pert PRO of PANalytical diffractometer using Cu Kα (=0.15406 nm) radiation. TEM and high-resolution TEM (HRTEM) images, selected area electron diffraction (SAED) patterns were collected using JEOL 2100 keV ultrahigh resolution field emission gun (UHR-FEG) TEM with voltage 200 keV. Aberration corrected high-angle annular dark-field scanning transmission electron microscopy (HAADF-STEM) as well as EDS mapping images were also collected using JEOL UHR-FEG TEM, operating at 200 kV. Samples for these measurements were prepared by dropcasting a small volume of sonicated nanocrystalline powders in ethanol onto a carbon-coated gold (Au) grid. Quantitative microanalysis on all the samples was performed using field-emission scanning electron microscopy (FESEM; JEOL, JSM-6700F instrument) equipped with an EDAX instrument. Data were acquired with an accelerating voltage of 20 kV and a 100 s accumulation time. X-ray photoelectron spectroscopy (XPS) measurements of all the samples were performed on an Omicron instrument, model 1712-62-11, using Al−Kα radiation source under 15 kV voltages and 5 mA current.

Catalyst Preparation and Electrochemical Studies: 2.00 mg of as synthesized catalysts was dispersed in 1 mL of mixed solvent solution (IPA/H_2O = 1:1 v/v) with 20 µL of 1 wt % nafion binder to prepare the catalyst ink. The nafion binder (5 wt%) was diluted to 1 wt% using isopropyl alcohol (IPA). From the prepared catalyst ink 10 µL was drop casted on GC electrode (3 mm diameter) and dried in air. Before depositing the catalyst, the GC electrode was polished with 0.05 µm alumina slurry, washed several times with distilled water. Commercial Pd/C (20 wt%, Alfa Aesar) was used for comparison of activity with the synthesized catalysts. In all the cases catalyst loading was maintained same (0.1 mg_{Pd}/cm^2).

All of the electrochemical measurements were carried out on CHI 6087E electrochemical workstation with three electrode setup at room temperature with GC as the working electrode, platinum wire as counter electrode, and Hg/HgO as the reference electrode. The electrolyte solution was deaerated by purging nitrogen gas into the solution at least 45 min before conducting each measurement.

Computational Details:

All the spin-polarized calculations were performed within the framework of density functional theory (DFT) based on first-principle calculations using the plane-wave technique as implemented in Vienna Ab initio Simulation Package (VASP).[1] The exchange-correlation energy was accounted within the generalized gradient approximation method (GGA) parametrized by the Perdew–Burke–Ernzerhof (PBE).[2] The onsite coulomb interaction "U" term (DFT+U method) was used to improve the description of localized Co, Ni, Cu d-electrons in $PdCu_3$ and substituted $PdCu_3$ surfaces with U_{eff} = 3.52, 4.0 and 7.0 eV as recommended by the previous studies.[3-5] The ion-electron interactions were treated using the projector augmented wave potential (PAW). Empirical correction method proposed by Grimme (DFT-D2) was adopted to describe the effect of van der Waals interactions.[6] In all computations, the kinetic energy cut off was set to be 500 eV in the plane-wave expansion. All the structures were fully relaxed (lattice constant and atomic position) using the conjugated gradient method and the convergence threshold was set to be 10^{-4} eV in energy and 0.01 eV/Å in force. For geometry optimization, The Brillouin zone was sampled with 5×5×1 and 7×7×1 Monkhorst-Pack k-point mesh respectively for geometry optimization and density of states (DOS) computation. For structure optimization of the small molecules such as CH_3CH_2OH, CH_3CO and OH in gas phase, we used B3LYP/6-31+G (d,p) method as implemented in Gaussian 16.[7] The climbing image nudge elastic band method (CI-NEB) was used to calculate activation barriers and six intermediate images were considered along the minimum energy path (MEP) to search for transition states for the EOR rate-determining step.[8] The MEPs were confirmed by phonon frequency calculations of the transition state (TS) along the diffusion coordinate at G points, which exhibits three N-3 real frequencies for reactants and or/products whereas those for TS three N-4 modes are real and one imaginary frequency. For all the pathways, activation barriers ($\Delta E^{\ddagger}$) were calculated using the following equations: $\Delta E^{\ddagger} = E_{TS} - E_{IS}$ and $\Delta E = E_{FS} - E_{IS}$, where IS, TS, and FS correspond to initial state, transition state, and final state, respectively. The formation energy was calculated according to the following equation

$$E_f = \frac{E_{Pd_{20-x}M_{x+y}Cu_{60-y}(111)} - [E_{Pd_{20}Cu_{60}(111)} - xE_{Pd} - yE_{Cu} + (x+y)E_{Co/Ni}]}{x+y}$$

Where $E_{Pd_{20-x}M_{x+y}Cu_{60-y}(111)}$, $E_{Pd_{20}Cu_{60}(111)}$, E_{Pd}, E_{Cu}, E_{Co}, E_{Ni} were the energies of the Co, Ni substituted $PdCu_3(111)$, pristine $PdCu_3(111)$ surfaces, isolated Pd, Cu, Co and Ni atoms respectively. x and y represented the no of Pd and Cu atoms substituted with either Ni or Co respectively.

The binding energy (E_{BE}) of the intermediates on various surfaces could be calculated as

$$E_{BE} = E_{adsorbate\,/\,surface} - E_{surface} - E_{adsorbate}$$

Where $E_{(adsorbate/surface)}$, $E_{surface}$ and $E_{(adsorbate)}$ were the total energies of adsorbed, pristine surfaces and adsorbates respectively.

According to HRTEM analysis, surface exposed plane for all the catalysts was (111). In order to model $PdCu_3(111)$ and PdM_xCu_{3-x} (M=Co, Ni; x=0.1, 03, 0.5) (111) surfaces, we considered a periodic five layered slabs with 2 × 2 surface cell (10.23 × 10.23 $Å^2$) with 80 atoms while that for Pd (111), a five-layered 4 × 4 surface cell (10.23 × 10.23 $Å^2$) with 80 atoms were considered. To avoid the spurious interactions between the neighboring slabs, a

vacuum layer of 20 Å was used in the direction perpendicular to the surfaces (along Z-direction) and the nearest distance between the two adsorbed molecules in the adjacent supercell was ~9 Å. For the substitution of Co and Ni atom at Cu atomic position, we considered the top two layers of five layered slab of $PdCu_3$ (111) surface as the first two layers could be considered as active surface while the three bottom layers as bulk. [9]

Table S1. List of particle size (determined from Scherrer formula) and lattice constants of all the catalysts.

Catalysts	Particle size (nm)	Lattice constant (nm)
Commercial Pd/C	3.6	0.3902
Disordered $PdCu_3$	3.5	0.3716
Ordered $PdCu_3$	4.2	0.3724
Ordered $PdCo_{0.3}Cu_{2.7}$	4.8	0.3695
Ordered $PdNi_{0.3}Cu_{2.7}$	4.3	0.3689

Table S2. ICP-AES data of all the catalysts.

Sample	**Pd**	**Cu**	**Co**	**Ni**
Disordered $PdCu_3$	26.75	73.25	-	-
Ordered $PdCu_3$	26.95	73.05	-	-
$PdNi_{0.1}Cu_{2.9}$	27.24	70.64	-	2.12
$PdNi_{0.3}Cu_{2.7}$	27.35	65.51	-	7.14
$PdNi_{0.5}Cu_{2.5}$	26.91	60.11	-	12.98
$PdCo_{0.1}Cu_{2.9}$	27.12	70.49	2.39	-
$PdCo_{0.3}Cu_{2.7}$	26.68	65.87	7.45	-
$PdCo_{0.5}Cu_{2.5}$	27.45	58.89	13.66	-

Calculation: Let a, b, c and d can be considered as the mg/10mL concentration of the Pd, Cu, Co and Ni respectively [for $PdCu_3$: c, d is considered as zero; $PdCo_xCu_{3-x}$ (x=0.1, 0.2, 0.3): d is considered as zero; $PdNi_xCu_{3-x}$ (x=0.1, 0.2, 0.3): c is considered as zero].

$$\%Pd = \frac{a}{a+b+c+d} \times 100$$

$$\%Cu = \frac{b}{a+b+c+d} \times 100$$

$$\%Co = \frac{c}{a+b+c+d} \times 100$$

$$\%\,\mathrm{Ni} = \frac{d}{a+b+c+d} \times 100$$

Table S3. Formation Energy of Co and Ni substitution at different Wyckoff sites of ordered $PdCu_3$ (111) surface.

(111) Surface	Model Surface	%substitution	Formation Energy (E_f) (eV)	
			Pd Site (1a)	Cu Site (3c)
$PdNi_{0.1}Cu_{2.9}$	$Pd_{20}Ni_2Cu_{58}$	2.5	-0.56	-1.65
$PdCo_{0.1}Cu_{2.9}$	$Pd_{20}Co_2Cu_{58}$	2.5	-0.07	-1.06

Table S4. Formation Energy of Co and Ni substitution at Cu site (Wyckoff site:3c) of substituted $PdCu_3$ (111) surface with varying concentration of substitution.

(111) Surface	Model Surface	%substitution	Formation Energy (E_f) (eV) at Cu Site (3c)
$PdNi_{0.1}Cu_{2.9}$	$Pd_{20}Ni_2Cu_{58}$	2.5	-1.65
$PdNi_{0.3}Cu_{2.7}$	$Pd_{20}Ni_6Cu_{54}$	7.5	-1.77
$PdNi_{0.5}Cu_{2.5}$	$Pd_{20}Ni_{10}Cu_{50}$	12.5	-1.43
$PdCo_{0.1}Cu_{2.9}$	$Pd_{20}Co_2Cu_{58}$	2.5	-1.06
$PdCo_{0.3}Cu_{2.7}$	$Pd_{20}Co_6Cu_{54}$	7.5	-1.60
$PdCo_{0.5}Cu_{2.5}$	$Pd_{20}Co_{10}Cu_{50}$	12.5	-1.58

Table S5. Composition of elements obtained from XPS analysis.

Sample	Pd (At.%)	Cu (At.%)	Co (At.%)	Ni (At.%)
Ordered $PdCu_3$	28.1	71.9	-	-
$PdCo_{0.3}Cu_{2.7}$	27.8	63.5	8.7	-
$PdNi_{0.3}Cu_{2.7}$	27.4	65.8	-	6.8

Table S6. Summary of the ratios of Pd/Pd^{n+} and Cu/Cu^{n+} for all the catalysts obtained from XPS analysis.

Catalysts	Pd/Pd^{n+} ratios	Cu/Cu^{n+} ratios
Ordered $PdCu_3$	4.7:1	4.4:1
$PdCo_{0.3}Cu_{2.7}$	2.5:1	3.0:1
$PdNi_{0.3}Cu_{2.7}$	2.9:1	2.4:1

Table S7. Electrochemically active surface area (ECSA) determined from PdO reduction region.

Catalysts	**ECSA (cm^2)**
Commercial Pd/C	2.63
Disordered $PdCu_3$	0.76
Ordered $PdCu_3$	1.10
$PdCo_{0.1}Cu_{2.9}$	1.08
$PdCo_{0.3}Cu_{2.7}$	1.12
$PdCo_{0.5}Cu_{2.5}$	0.96
$PdNi_{0.1}Cu_{2.9}$	1.06
$PdNi_{0.3}Cu_{2.7}$	1.16
$PdNi_{0.5}Cu_{2.5}$	0.97

Table S8. Comparison of EOR activity in alkaline electrolyte (similar condition, scan rate: 50 mV/s; 1 M ethanol concentration) for ordered $PdCu_3$ and $PdNi_{0.3}Cu_{2.7}$ with other state-of-the-art electrocatalysts.

Catalysts	Specific Activity (mA/cm^2)	Mass Activity (A/mg_{pd})	References
Pd–PEDOT/graphene	3.5	0.46	[10]
Pd/PANI/Pd SNTAs	-	0.36	[11]
Pd_3Pb	2.02	0.51	[12]
Pd_2Ge	4.64	-	[13]
Cu_xPd_y/carbon	-	0.52	[14]
NiNWA/PdNF	1.7	0.77	[15]
PdCuSn/CNTs	-	0.87	[16]
Activated PdCu/3DGS	-	1.14	[17]
$Pd/Ni(OH)_2$/rGO	-	1.5	[18]
CuO/Pd	4.35	2.01	[19]
$Pd_{1.6}Ni_{0.4}Ge$	12.94	0.89	[20]
Ordered $PdCu_3$	**8.1**	**1.24**	**This Work**
Ordered $PdNi_{0.3}Cu_{2.7}$	**13.0**	**2.1**	**This Work**
Pd/GC-V_8C_7	-	3.54	[21]
$Pd_{86}Sn_{14}$/C	8.4	-	[22]
$Pd_{40}Ni_{43}P_{17}$	-	4.95	[23]
Pd_3Pb/C (8 nm cube)	20	2.05	[24]

Table S9. Adsorption Energies of OH, CH_3CO and CO on different surfaces.

Catalysts	Adsorption Energies (Eads) (in eV)		
	OH	**CH_3CO**	**CO**
Commercial Pd/C	-2.53	-2.90	-1.22
Ordered $PdCu_3$	-2.95	-2.79	-0.81
$PdNi_{0.1}Cu_{2.9}$	-3.03	-2.44	-0.42
$PdNi_{0.3}Cu_{2.7}$	-3.45	-2.10	-0.33
$PdNi_{0.5}Cu_{2.5}$	-3.21	-2.27	-0.57
$PdCo_{0.3}Cu_{2.7}$	-3.35	-2.21	-0.48

Table S10. The position of DBCs for different catalysts (111) surfaces.

Catalysts	Position of DBCs (in eV) of Pd
Commercial Pd/C	-1.80
Ordered $PdCu_3$	-1.95
$PdNi_{0.1}Cu_{2.9}$	-2.07
$PdNi_{0.3}Cu_{2.7}$	-2.10
$PdNi_{0.5}Cu_{2.5}$	-2.04
$PdCo_{0.3}Cu_{2.7}$	-2.14

Table S11. The activation energy barriers ($\Delta E^{\ddagger}$) of CH_3COOH formation and desorption for catalysts (111) surfaces.

Catalysts	Activation Barrier ($\Delta E^{\ddagger}$) (eV)	
	CH_3COOH Formation	**CH_3COOH Desorption**
Commercial Pd/C	0.60	0.22
Ordered $PdCu_3$	0.42	0.19
$PdNi_{0.1}Cu_{2.9}$	0.32	0.18
$PdNi_{0.3}Cu_{2.7}$	0.22	0.16
$PdNi_{0.5}Cu_{2.5}$	0.35	0.20
$PdCo_{0.3}Cu_{2.7}$	0.30	0.17

Table S12. Distance between "C" atom of CH_3CO and "O" atom of OH in the r.d.s CH_3COOH formation of both IS and TS for different catalyst surfaces.

Catalysts	Distance between "C" atom of CH_3CO and "O" atom of OH (Å)	
	Initial State (IS)	**Transition State (TS)**
Commercial Pd/C	2.70	2.35
Ordered $PdCu_3$	2.55	2.24
$PdNi_{0.1}Cu_{2.9}$	2.38	1.98
$PdNi_{0.3}Cu_{2.7}$	2.22	1.91
$PdNi_{0.5}Cu_{2.5}$	2.47	2.06
$PdCo_{0.3}Cu_{2.7}$	2.36	1.97

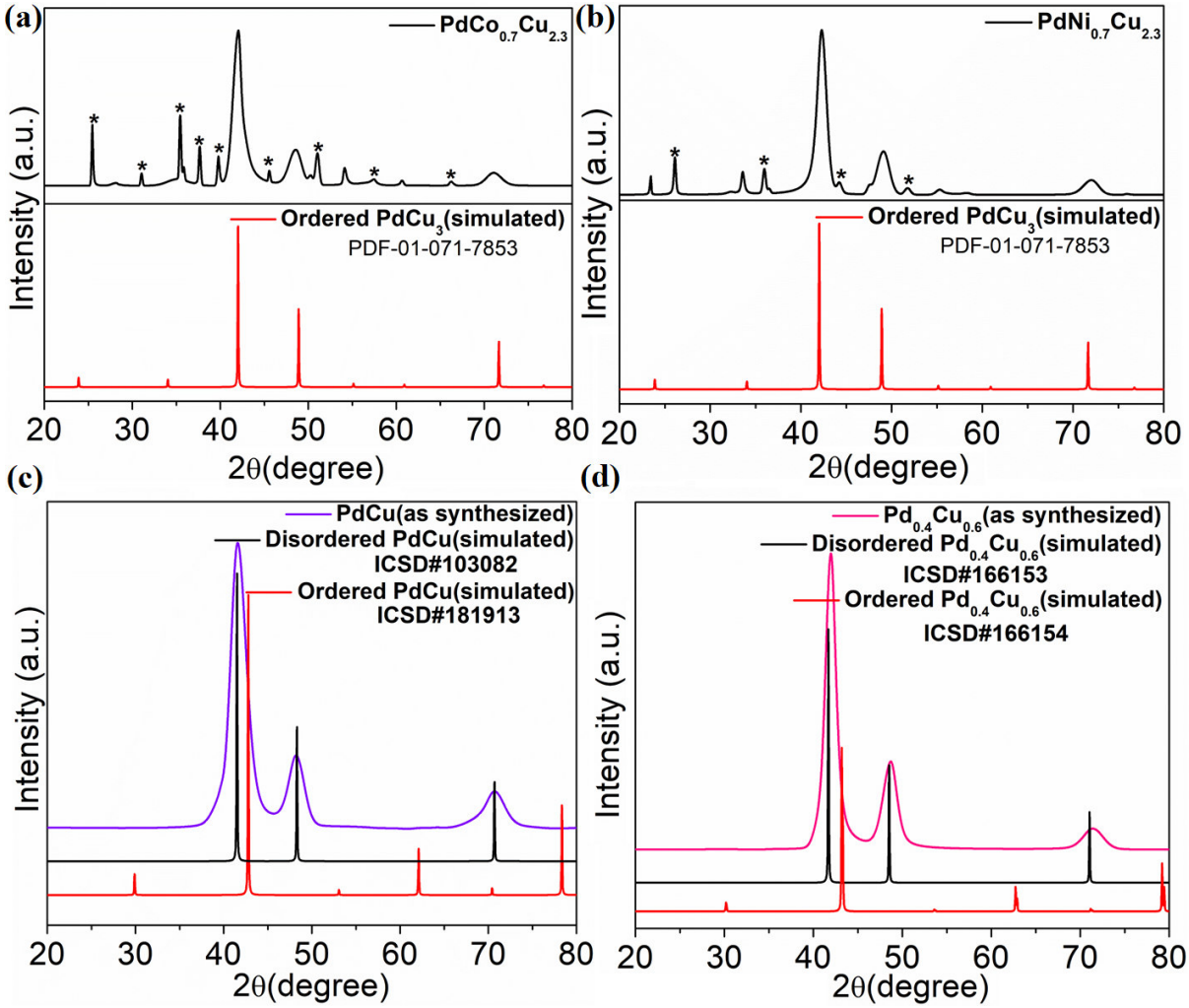

Fig. S1 Powder XRD patterns of the synthesized catalysts with the simulated patterns[25-28] (a) $PdCo_{0.7}Cu_{2.3}$, (b) $PdNi_{0.7}Cu_{2.3}$, (c) disordered PdCu, (d) disordered $Pd_{0.4}Cu_{0.6}$.

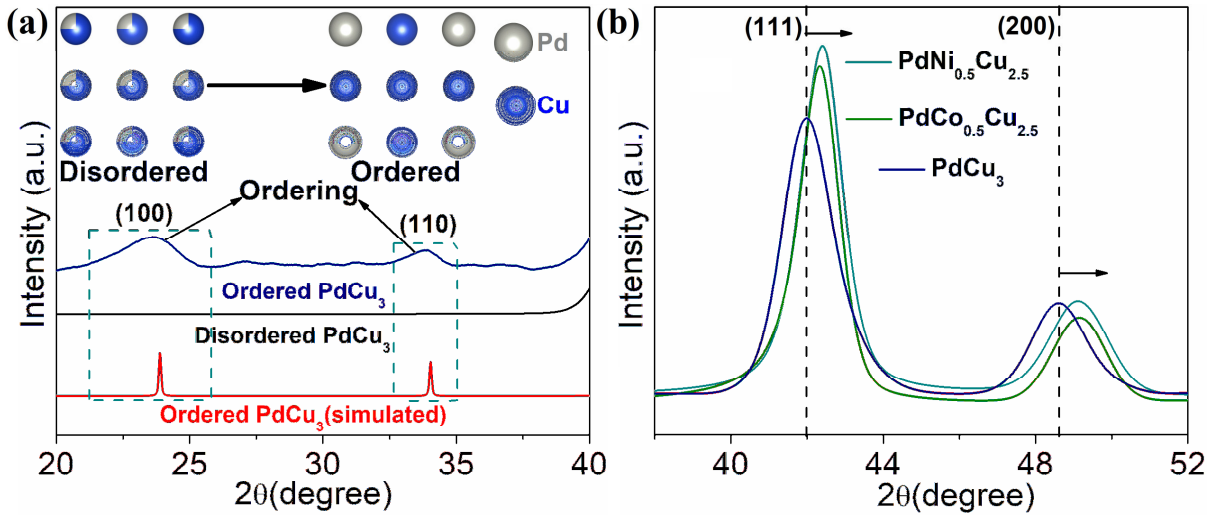

Fig. S2 (a) Enlarged view of the (111) and (200) peaks to visualize the shift after substitution (inset shows crystal structure of ordered and disordered $PdCu_3$), (b) Enlarged view of the (111) and (200) peaks to visualize the shift after substitution.

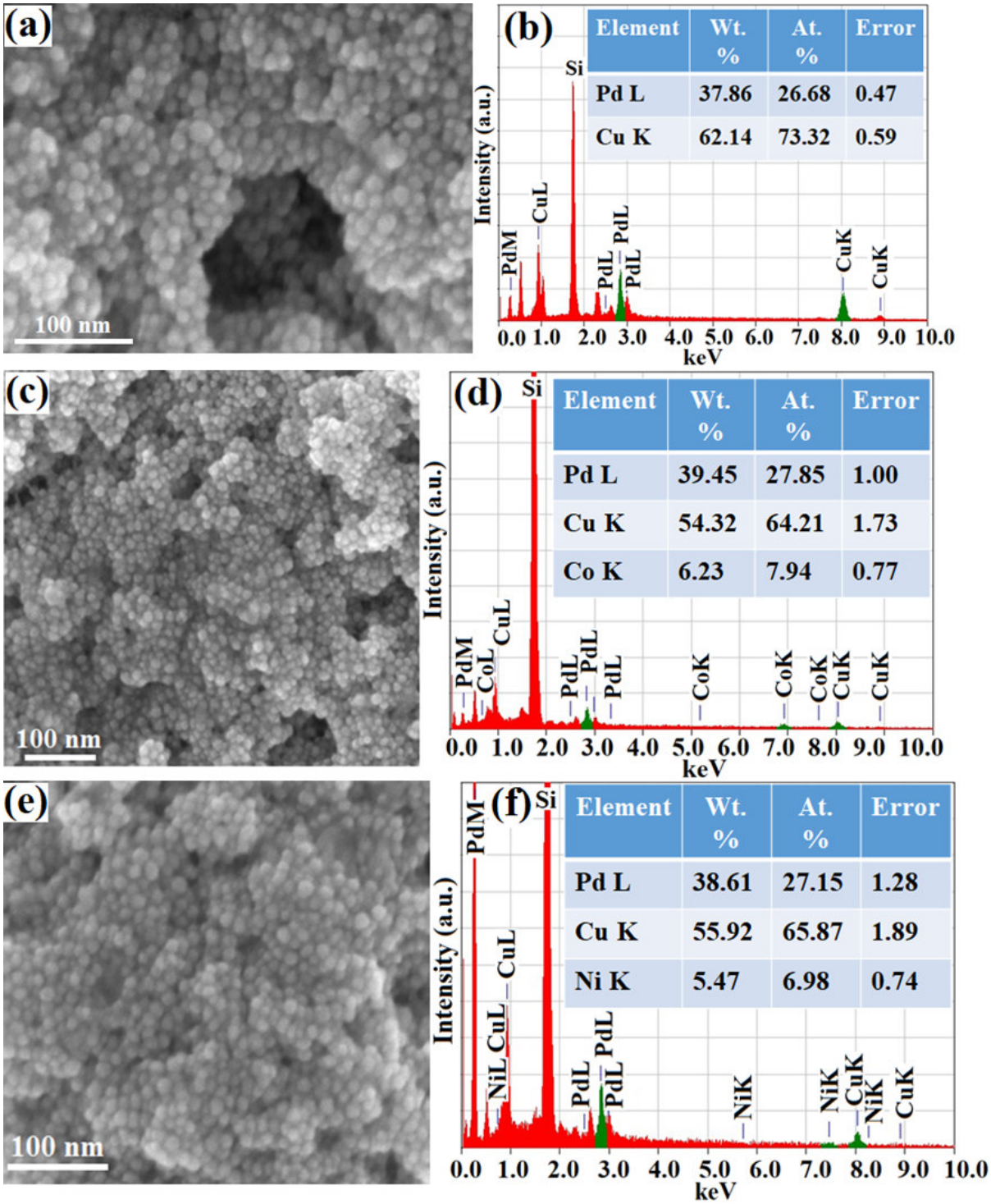

Fig. S3 FESEM micrographs and corresponding EDS data on different selected areas and spots of (a-b) ordered $PdCu_3$, (c-d) $PdCo_{0.3}Cu_{2.7}$, (e-f) $PdNi_{0.3}Cu_{2.7}$ NPs.

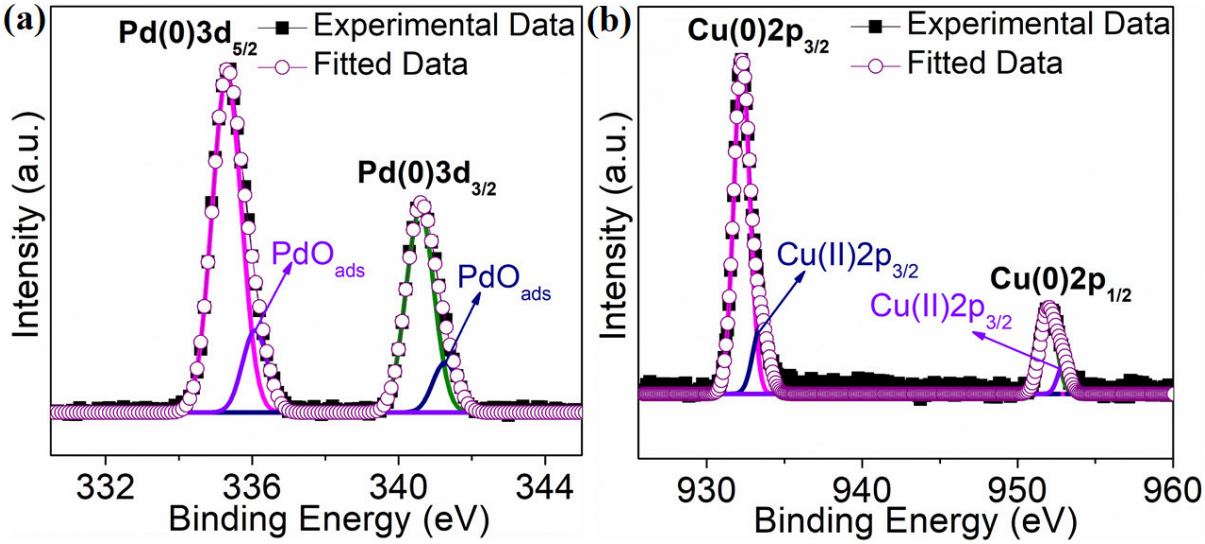

Fig. S4 Core level XPS spectra of ordered $PdCu_3$ NPs (a) Pd 3d, (b) Cu 2p.

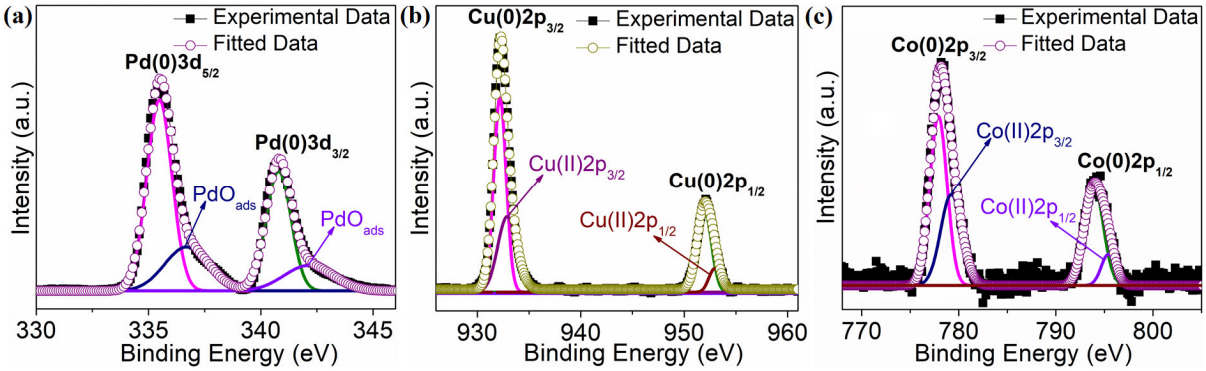

Fig. S5 Core level XPS spectra of $PdCo_{0.3}Cu_{2.7}$ NPs (a) Pd 3d, (b) Cu 2p, (c) Co 2p.

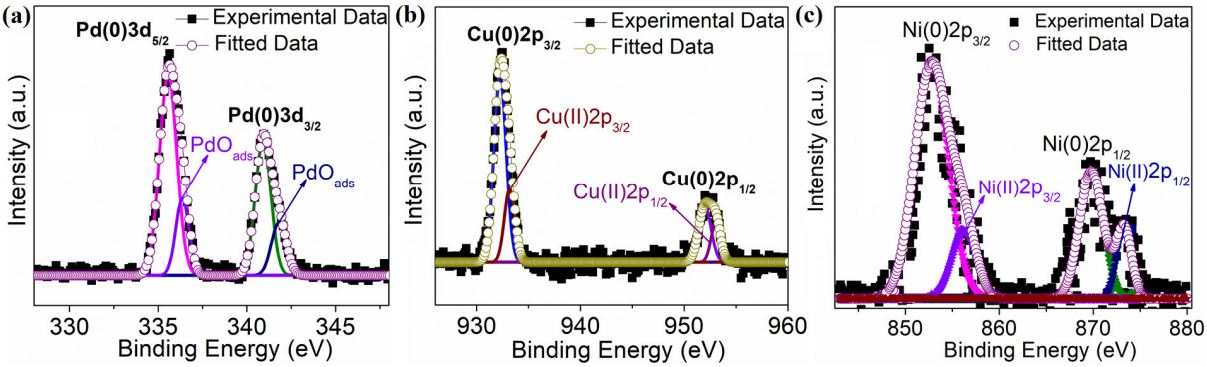

Fig. S6 Core level XPS spectra of $PdNi_{0.3}Cu_{2.7}$ NPs (a) Pd 3d, (b) Cu 2p, (c) Ni 2p.

XPS spectra of ordered $PdCu_3$, $PdCo_{0.5}Cu_{2.5}$ and $PdNi_{0.5}Cu_{2.5}$ NPs are shown in Fig. S4-6. Pd 3d peaks appearing at~335.5 ($3d_{5/2}$) and~340.8 eV ($3d_{3/2}$), Cu 2p peaks at ~932.2 ($2p_{3/2}$) and~ 952.1 eV ($2p_{1/2}$) and Co 2p peaks at ~778.2 ($2p_{3/2}$) and ~ 794 eV ($2p_{1/2}$) clearly suggests the presence of Pd(0), Cu(0) and Co(0) in the synthesized $PdCo_{0.5}Cu_{2.5}$ NPs while the higher energy peaks in XPS spectra can be assigned to PdO_{ads}, Cu(II) and Co(II) species. Ni 2p peaks at ~852.8 ($2p_{3/2}$) and ~869.7 eV ($2p_{1/2}$) indicates the presence of Ni(0) in $PdNi_{0.5}Cu_{2.5}$. The expected stoichiometric ratios of Pd, Cu, Ni and Co obtained from EDS and ICP-AES support XPS composition analysis (Table S2, S5 and Fig. S3). A detailed analysis of XPS data reveals that there is considerable change of Pd/Pd^{n+} and Cu/Cu^{n+} ratios in ordered $PdCu_3$ and $PdM_{0.3}Cu_{2.7}$ (M = Co, Ni) catalysts (Table S6). Decrease in Pd/Pd^{n+} and Cu/Cu^{n+} ratios are observed upon addition of Ni and Co in ordered $PdCu_3$. The reduced Pd/Pd^{n+} and Cu/Cu^{n+} ratios in $PdM_{0.3}Cu_{2.7}$ catalysts compared to $PdCu_3$ vividly demonstrate that substituted $PdM_{0.3}Cu_{2.7}$ consists of more amount of surface adsorbed PdO and CuO_x.

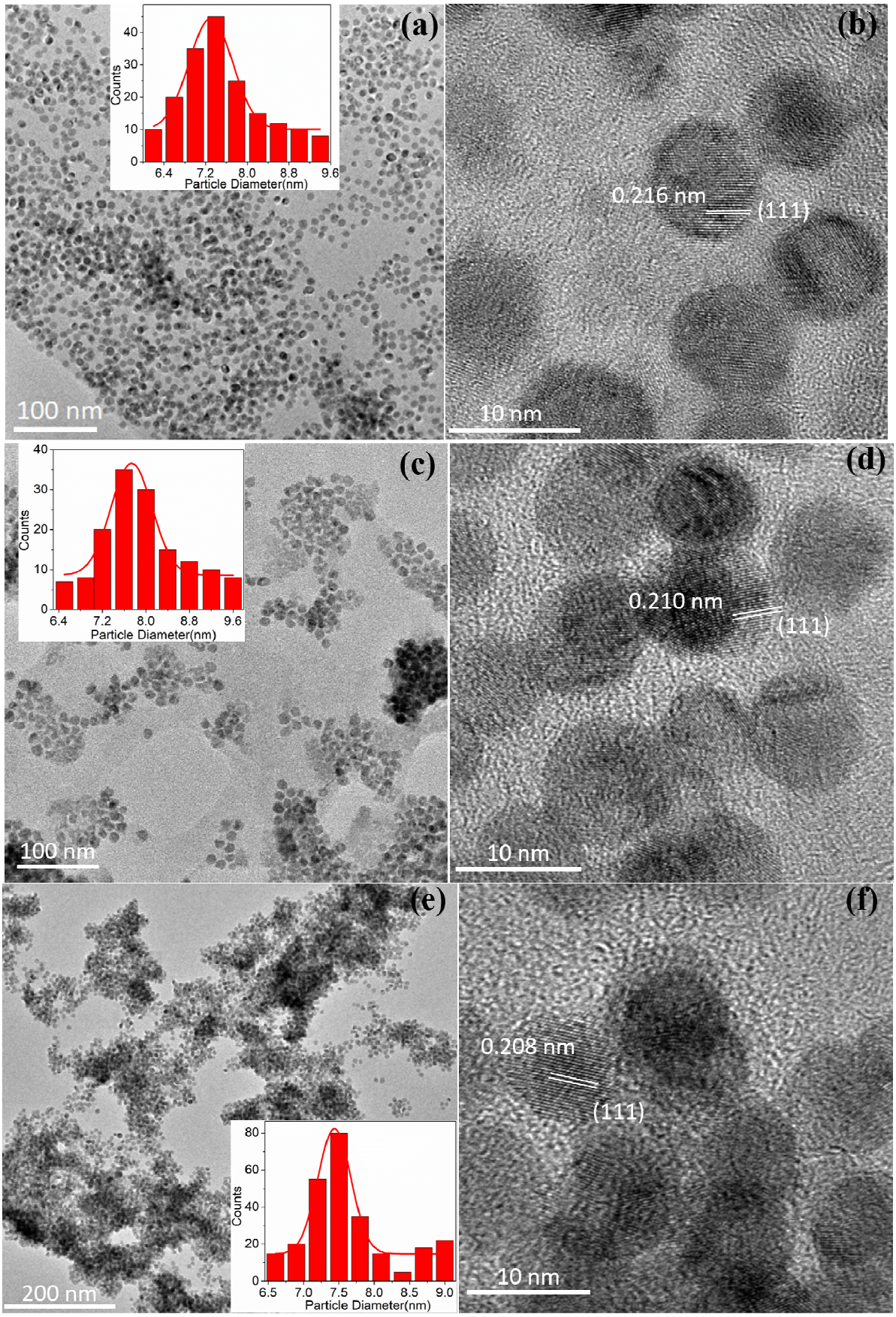

Fig. S7 TEM images (inset shows particle size distribution plots) and HRTEM images (a) $PdCu_3$, (c-d) $PdCo_{0.3}Cu_{2.7}$, (e-f) $PdNi_{0.3}Cu_{2.7}$ NPs.

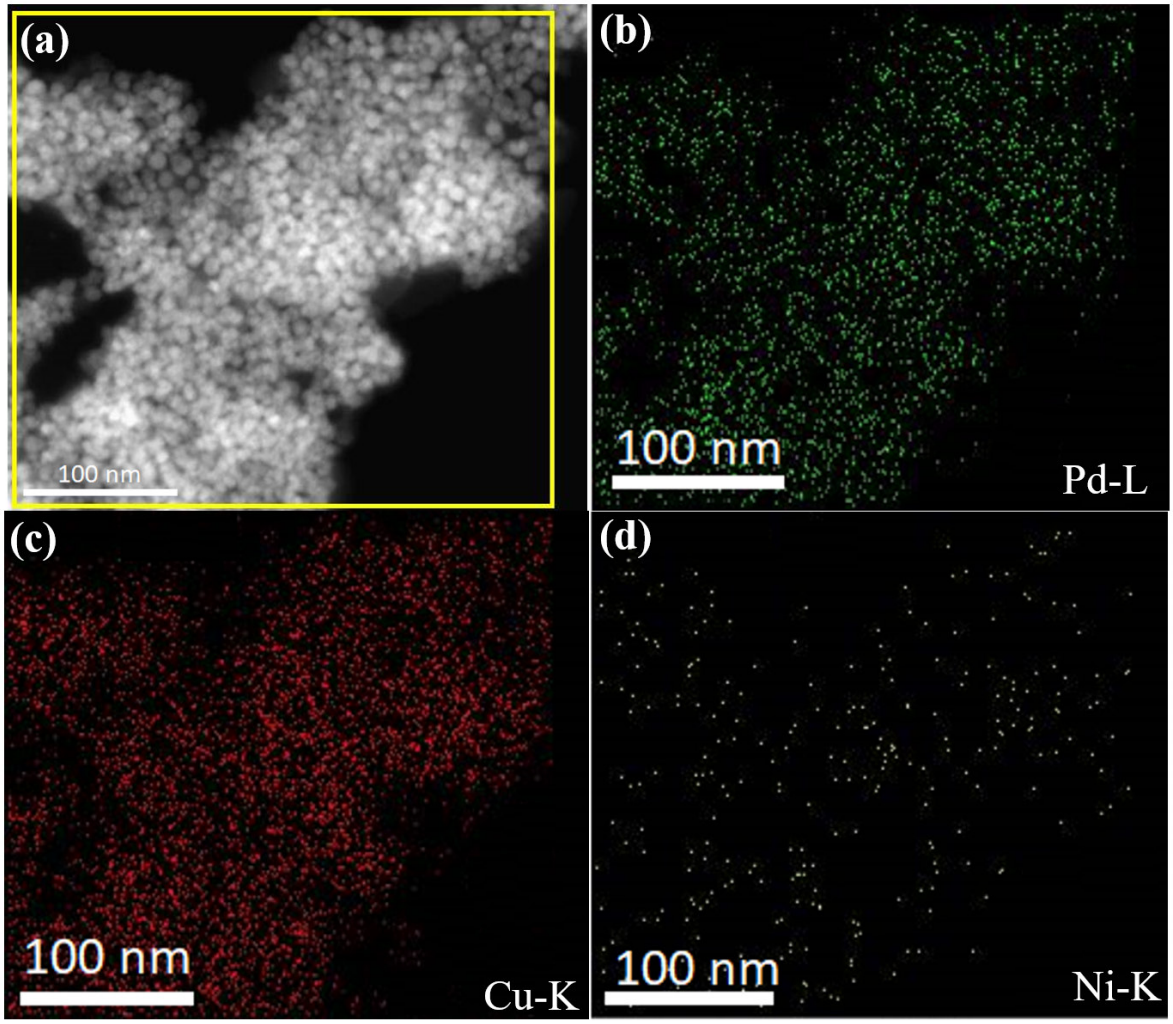

Fig. S8 (a) HAADF-STEM EDS elemental mapping (a) scan area, (b) Pd, (c) Cu , (d) Ni elemental map.

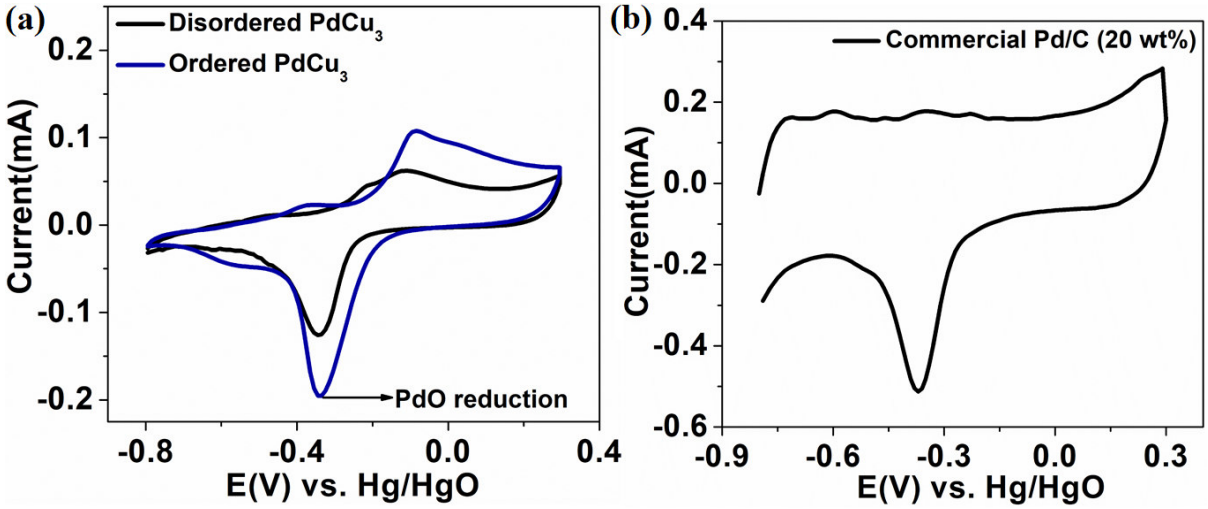

Fig. S9 Cyclic voltammetry measurements for (a) disordered and ordered $PdCu_3$, (b) commercial Pd/C (20 wt%) in 1 M KOH solution.

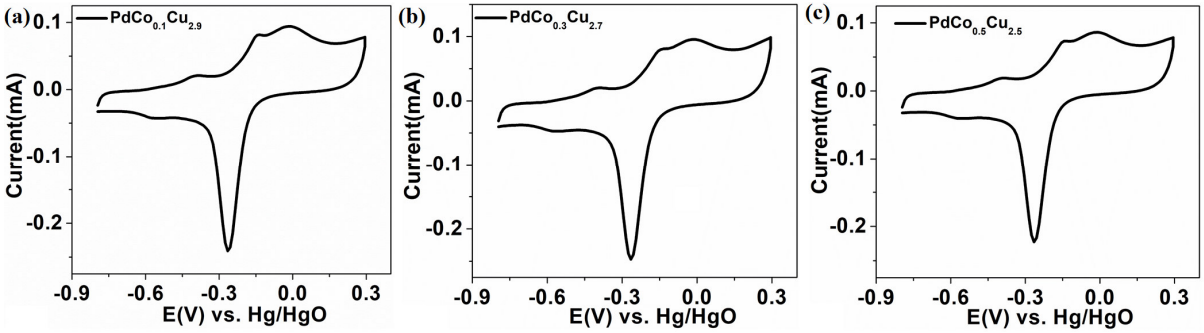

Fig. S10 Cyclic voltammetry measurements of $PdCo_xCu_{3-x}$ (x= 0.1, 0.3, 0.5) in 1 M KOH at a scan rate of 50 mV/s.

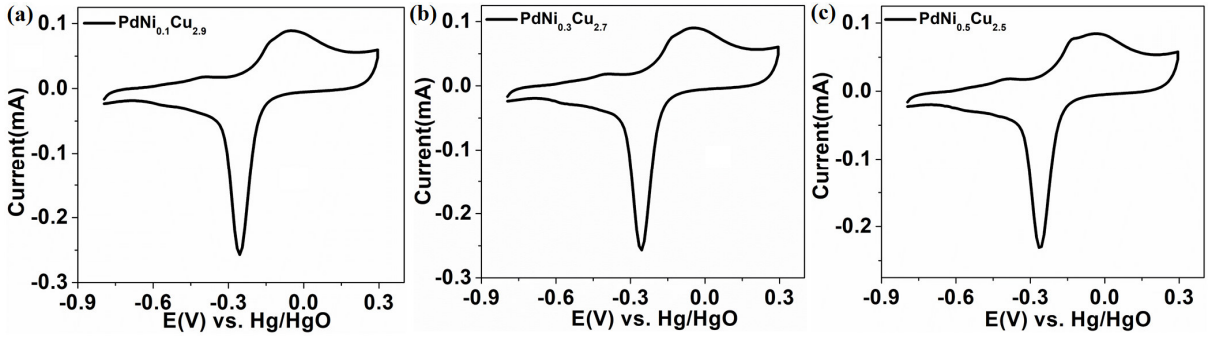

Fig. S11 Cyclic voltammetry measurements for $PdNi_xCu_{3-x}$ (x= 0.1, 0.3, 0.5) in 1 M KOH at a scan rate of 50 mV/s.

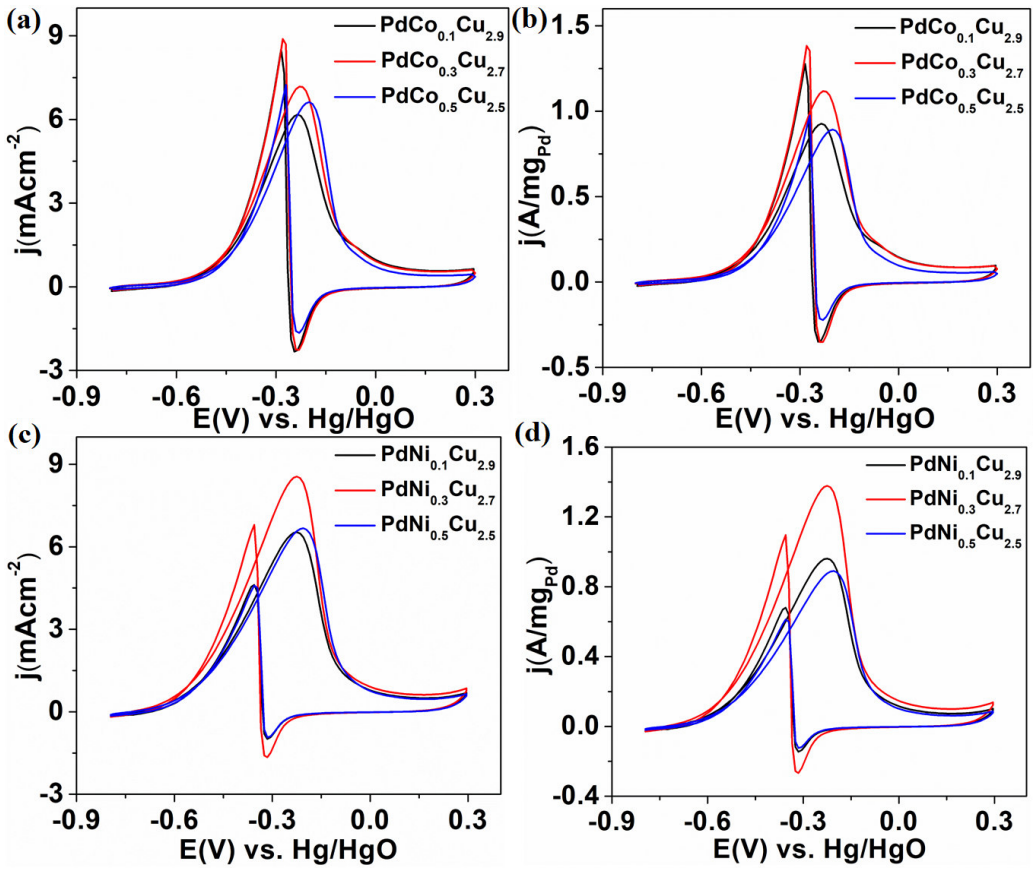

Fig. S12 Comparison of specific and mass activities of the catalysts (a-b) $PdCo_xCu_{3-x}$ (x= 0.1, 0.3, 0.5), (c-d) $PdNi_xCu_{3-x}$ (x= 0.1, 0.3, 0.5).

Increase of EOR activity with respect to substituent concentration does not occur linearly. Both $PdM_{0.5}Cu_{2.5}$ (M=Co, Ni) catalysts show a decrease in activity compared to its $PdM_{0.3}Cu_{2.7}$ (M=Co, Ni) analogue (Fig. S12). Fig. 3c overwhelmingly demonstrates the remarkable increase in specific and mass activities of the substituted analogues in comparison with pristine one. There are ~5.3 and ~2.2 times increase of specific and mass activity of ordered $PdCu_3$ when compared to commercial Pd/C (20 wt%) (Fig. 3a and c). The enhanced activity of $PdCu_3$ compared to Pd/C is attributed to the bi-functional and/or synergistic effect where more oxophilic Cu strongly interacts with OHads making Pd sites free for adsorption and dissociation of ethanol. Besides, combination of CH_3CO (adsorbed on Pd site) and OH radical (adsorbed on Cu site) promotes the generation of acetate ion in the rate determining step of EOR. However, in terms of specific activity, both $PdCo_{0.3}Cu_{2.7}$ and $PdNi_{0.3}Cu_{2.7}$ are respectively ~8 and ~9.4 times superior to commercial Pd/C (Fig. 3a and c). Mass activity of $PdCo_{0.3}Cu_{2.7}$ and $PdNi_{0.3}Cu_{2.7}$ catalysts are also respectively ~3.3 and ~4.1 times higher compared to Pd/C (inset of Fig. 3d). More interestingly, at 500^{th} cycle, Pd/C drastically loses its activity (~78% loss in mass and specific activity) while $PdCu_3$ and $PdM_{0.3}Cu_{2.7}$ (M=Co, Ni) exhibits respectively ~68%, ~ 61% and 59% gain in peak current density (Fig. 3b and c). After 500^{th} cycle, $PdCo_{0.3}Cu_{2.7}$ and $PdNi_{0.3}Cu_{2.7}$ demonstrates ~57 and ~65 times higher specific activity and ~25.5 and ~30 times higher mass activity compared to Pd/C. Similar trend has been also noticed in the mass activity for pristine and substituted $PdCu_3$. However, mass and specific activity of the catalysts increase upto 500^{th} cycles then start to decrease (Fig. S13). The reason for substantial enhancement of EOR activity of the Ni and Co-substituted catalysts may be attributed to the modification of electronic structure of the catalysts resulting optimized intermediate adsorption in close proximity. Besides, the presence of surface adsorbed PdO and CuO_x oxide layers can substantially enhance the EOR activity of Pd based systems due to alteration in adsorption properties of ethanol and other intermediate species. Hence increased amount of surface adsorbed PdO and CuO_x species in Co and Ni-substituted $PdCu_3$ remarkably enhance EOR activity. The comparison of EOR activity in alkaline media with other state-of-the-art catalysts are summarized in Table S8.

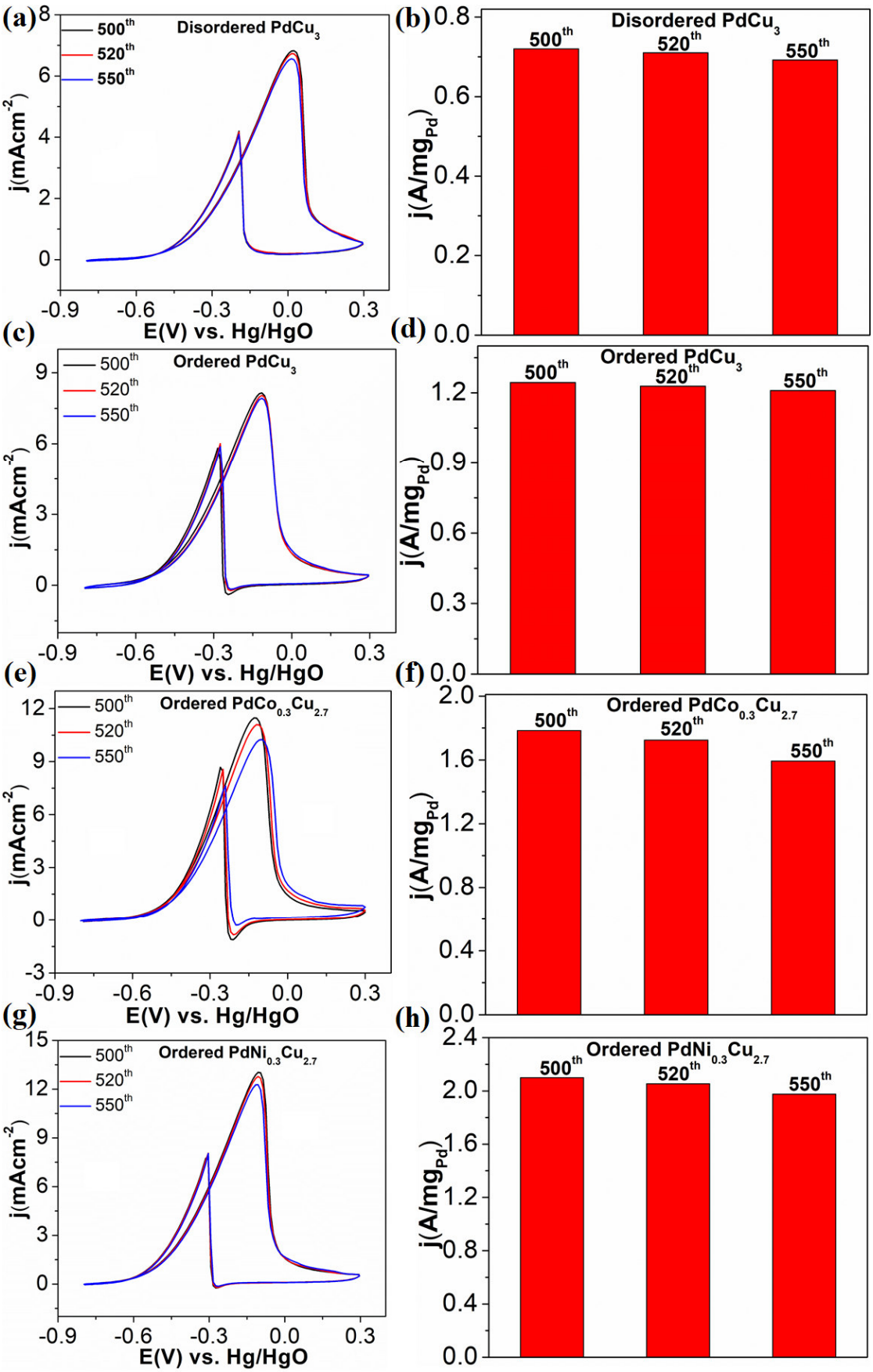

Fig. S13 Comparison of specific and mass activities of the catalysts at 500th, 520th, 550th cycles in 1M KOH solution containing 1 M ethanol.

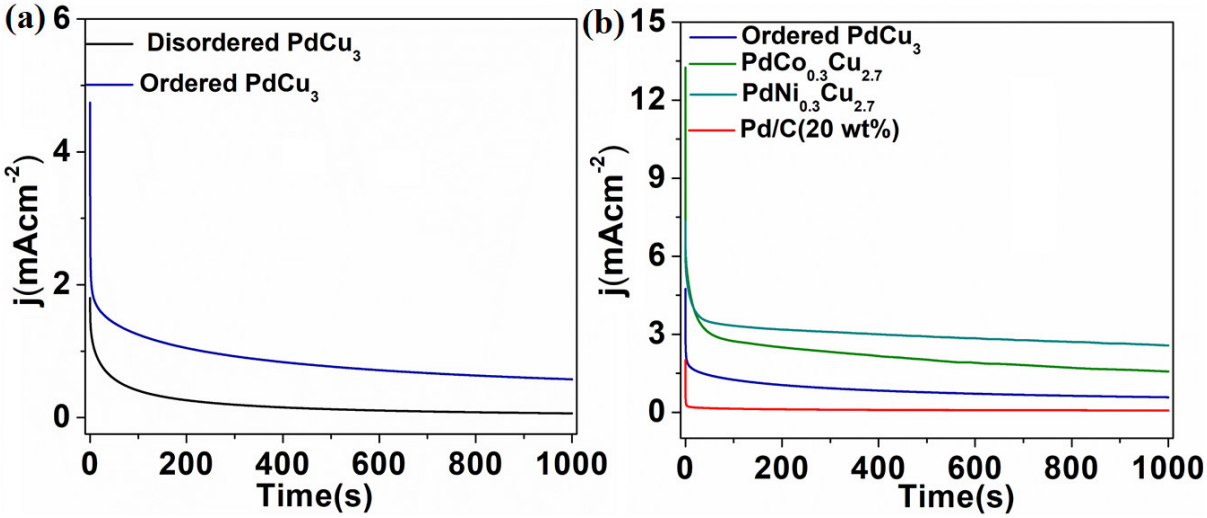

Fig. S14 Chronoamperometry (CA) study of the catalysts at -0.2 V vs Hg/HgO in 1 M KOH+ 1M ethanol solution for 1000s (a) disordered and ordered $PdCu_3$, (b) $PdCu_3$, substituted $PdCu_3$ and commercial Pd/C.

The stability of the catalysts have been evaluated through chronoamperometry (CA) measurement in 1 M KOH containing 1 M ethanol at applied potential of -0.2 V vs Hg/HgO for 1000s (Fig. S14). After initial decrease due to double layer discharge, a pseudo-steady state is reached and this steady-state current density is compared to evaluate the stability of the catalyst. As expected, stability of the ordered $PdCu_3$ is higher compared to disordered one due to uniformity of the ordered surface (fig. S14a). The stability of the ordered pristine and substituted $PdCu_3$ catalysts follows the trend: $PdCu_3 < PdCo_{0.3}Cu_{2.7} < PdNi_{0.3}Cu_{2.7}$.

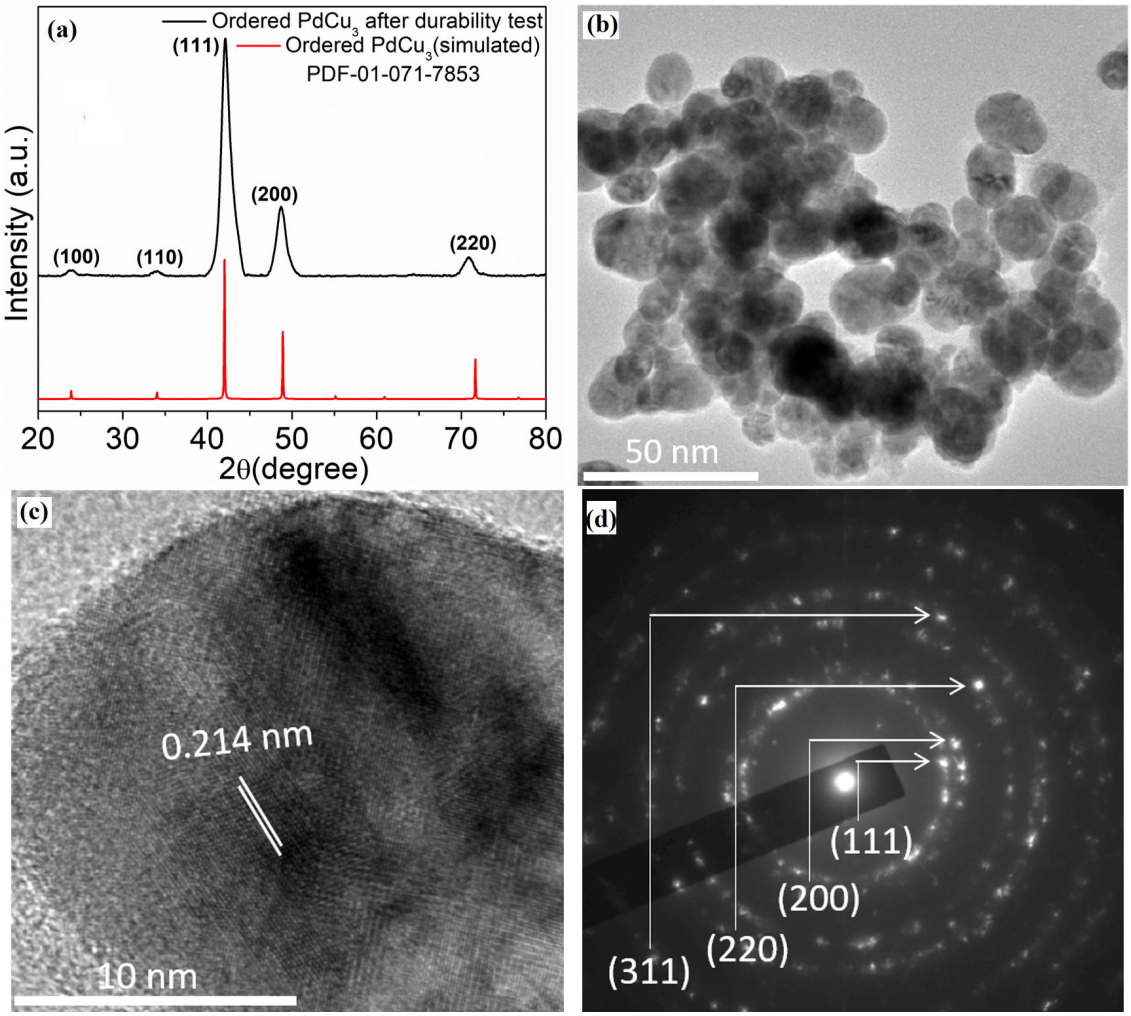

Fig. S15 (a) Comparison of PXRD pattern of post-catalytic ordered $PdCu_3$ with simulated pattern, (b) TEM image, (c) HRTEM image, (d) SAED pattern of ordered $PdCu_3$ after durability test.

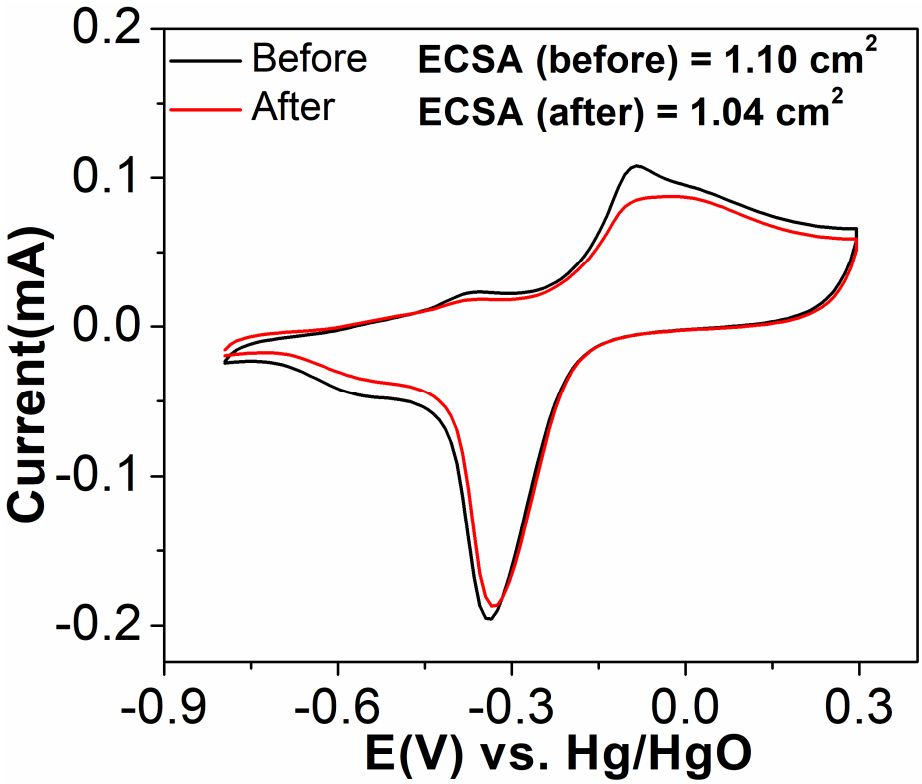

Fig. S16 Comparison of cyclic voltammetry measurements before and after durability test of ordered $PdCu_3$ catalyst.

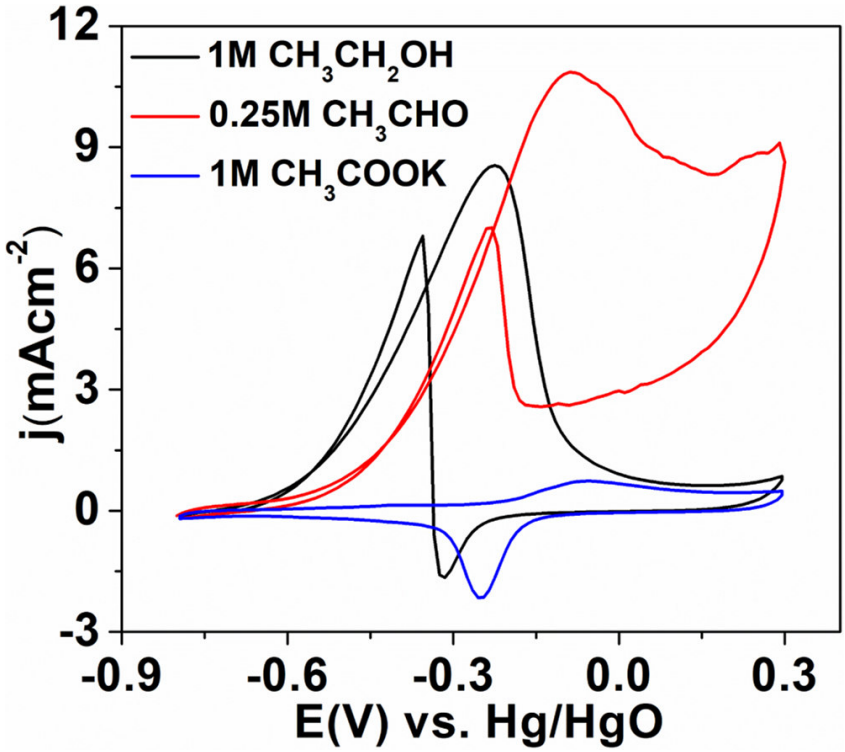

Fig. S17 Comparison of cyclic voltammograms of $PdNi_{0.3}Cu_{2.7}$ for the oxidation of ethanol (CH_3CH_2OH), acetaldehyde (CH_3CHO), acetic acid (CH_3COOH) in 1 M KOH solution at a scan rate 50 mV/s.

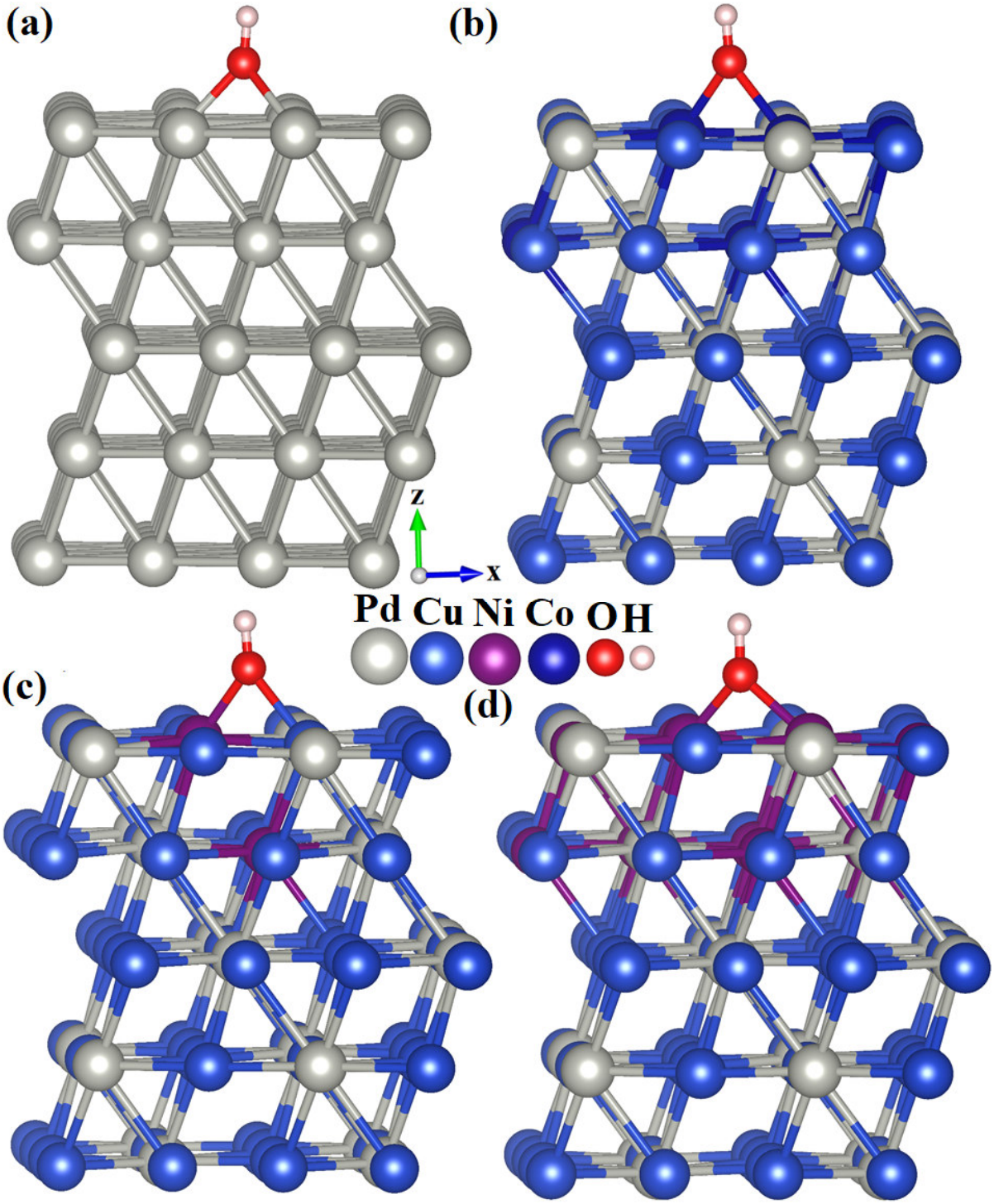

Fig. S18 OH adsorbed surfaces (a) Pd (111), (b) $PdCo_{0.3}Cu_{2.7}$ (111), (c) $PdNi_{0.1}Cu_{2.9}$ (111) and (d) $PdNi_{0.5}Cu_{2.5}$ (111).

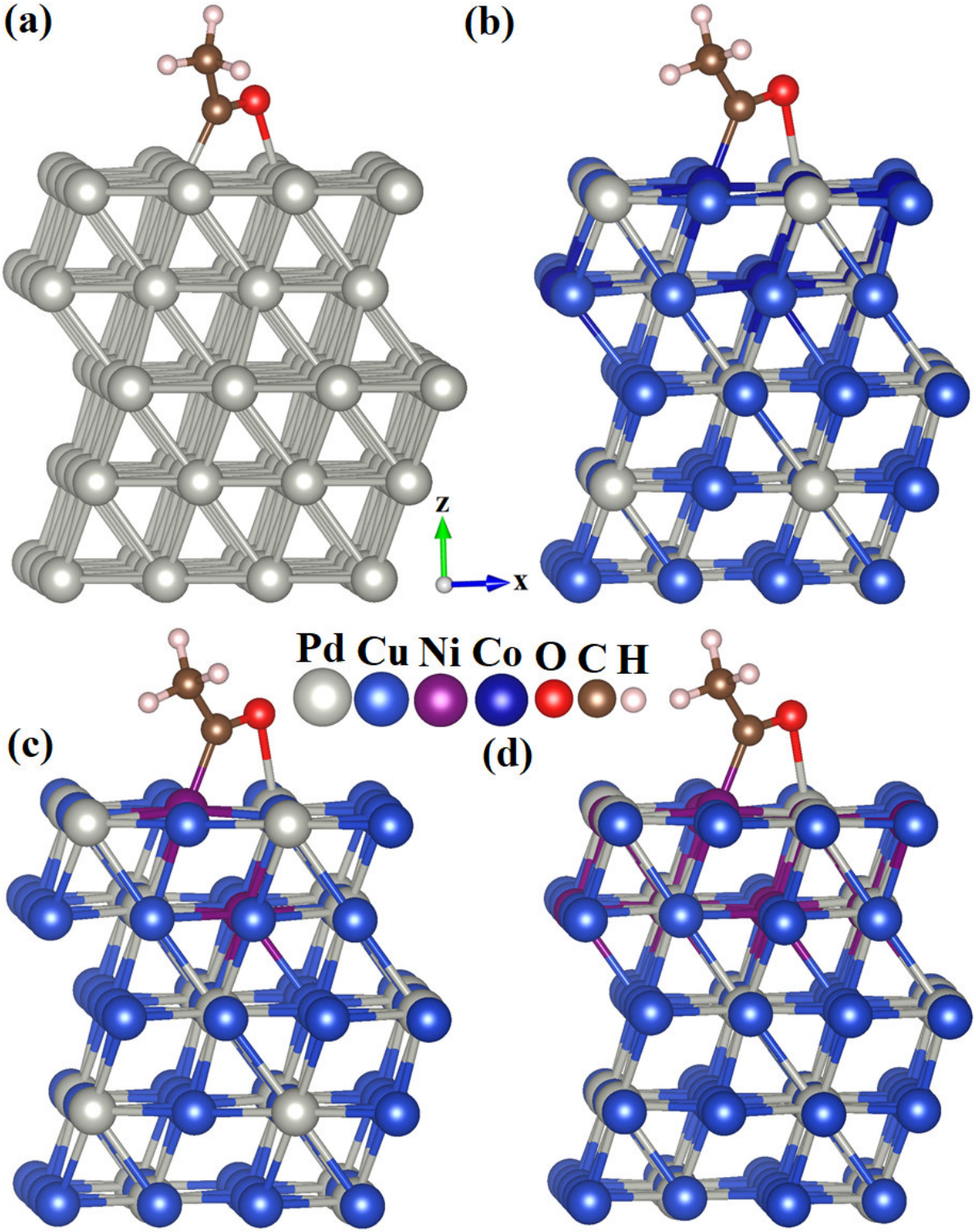

Fig. S19 CH_3CO adsorbed surfaces (a) Pd (111), (b) $PdCo_{0.3}Cu_{2.7}$ (111), (c) $PdNi_{0.1}Cu_{2.9}$ (111) and (d) $PdNi_{0.5}Cu_{2.5}$ (111).

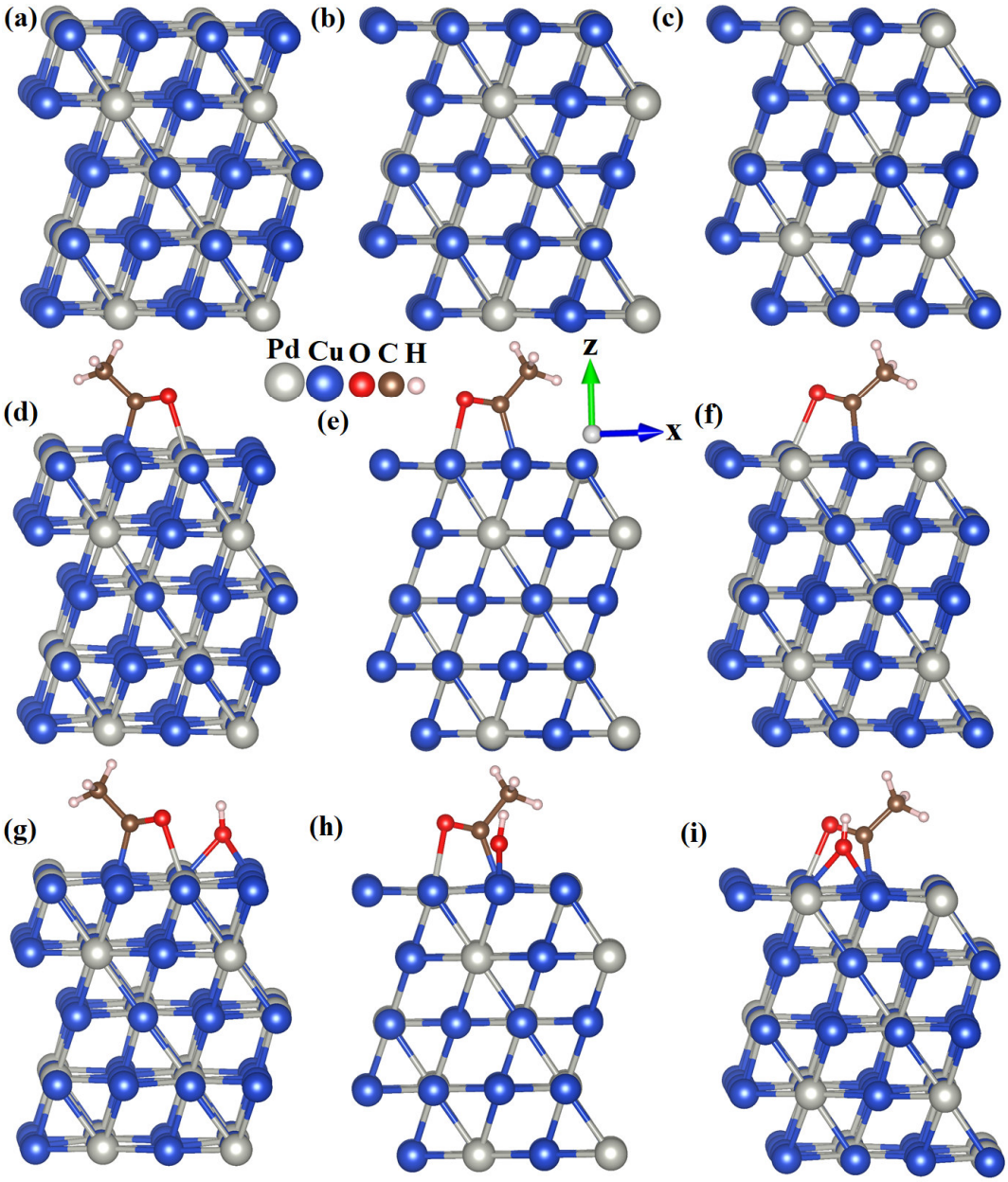

Fig. S20 (a-c) Different disordered $PdCu_3$ surfaces, (d-f) CH_3CO adsorbed disordered surfaces, (g-i) Both CH_3CO and OH adsorbed surfaces.

As there is no specific atomic site present in disordered alloys, the disordered surface may be represented as a combination of four probable $PdCu_3$ surfaces where ordered $PdCu_3$ is also one of the possible surfaces. As evident form Fig. S20, owing to non-uniformity of the active Pd site and secondary Cu site, there are substantial positional differences in the adsorption of CH_3CO and OH intermediates. Most importantly, intermediate adsorption is random in nature. Hence, site specific adsorption of intermediates on catalyst surface will be hindered leading to the reduction of EOR activity.

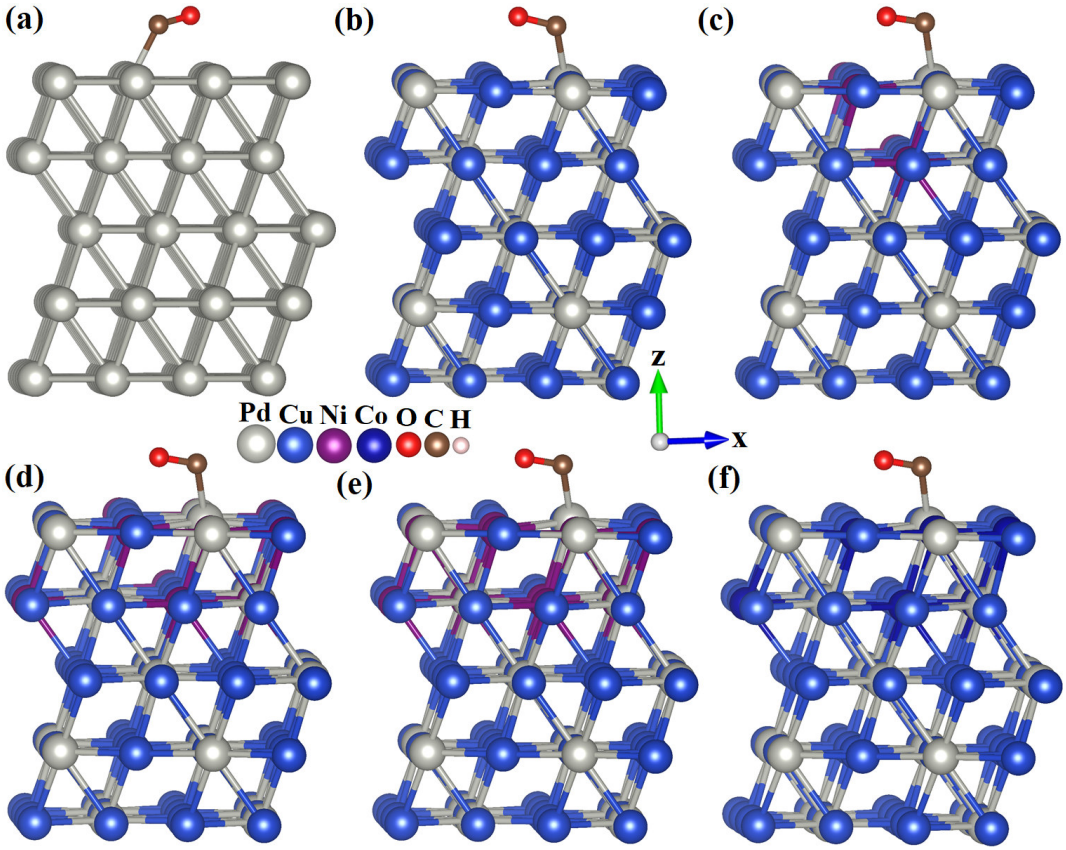

Fig. S21 Adsorption of CO on (111) surfaces of different catalysts (a) Pd, (b) $PdCu_3$, (c) $PdNi_{0.1}Cu_{2.9}$, (d) $PdNi_{0.3}Cu_{2.7}$, (e) $PdNi_{0.5}Cu_{0.5}$, (f) $PdCo_{0.3}Cu_{2.7}$.

Catalyst degradation due to surface poisoning by in-situ generated CO, can be well understood from CO adsorption energies. Relatively weaker CO adsorption on $PdNi_{0.3}Cu_{2.7}$ (111) proves that the surface is less prone to CO poisoning supported by CA study (Fig. S21 and Table S9).

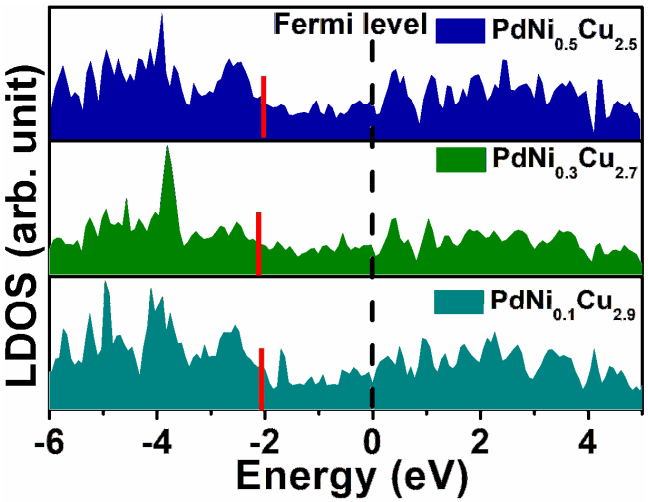

Fig. S22 Local Density of States (LDOS) plots on Pd atom for different catalysts (thick red bar indicates the position of d-band center (Ed) of Pd).

Well-known d-band model correlating the d-band center (DBC) with intermediate adsorption further justifies the EOR activity order. The optimal position of DBC with respect to Fermi level clearly indicates optimal intermediate adsorption on substituted $PdCu_3$ and hence enhanced EOR activity (Fig. 4e and Table S10). However further shift of DBC towards fermi level deteriorates the activity of $PdNi_{0.5}Cu_{2.5}$ (Fig. S22). This study also accounts for the necessity of optimal DBC position of a catalyst for moderate intermediate adsorption.

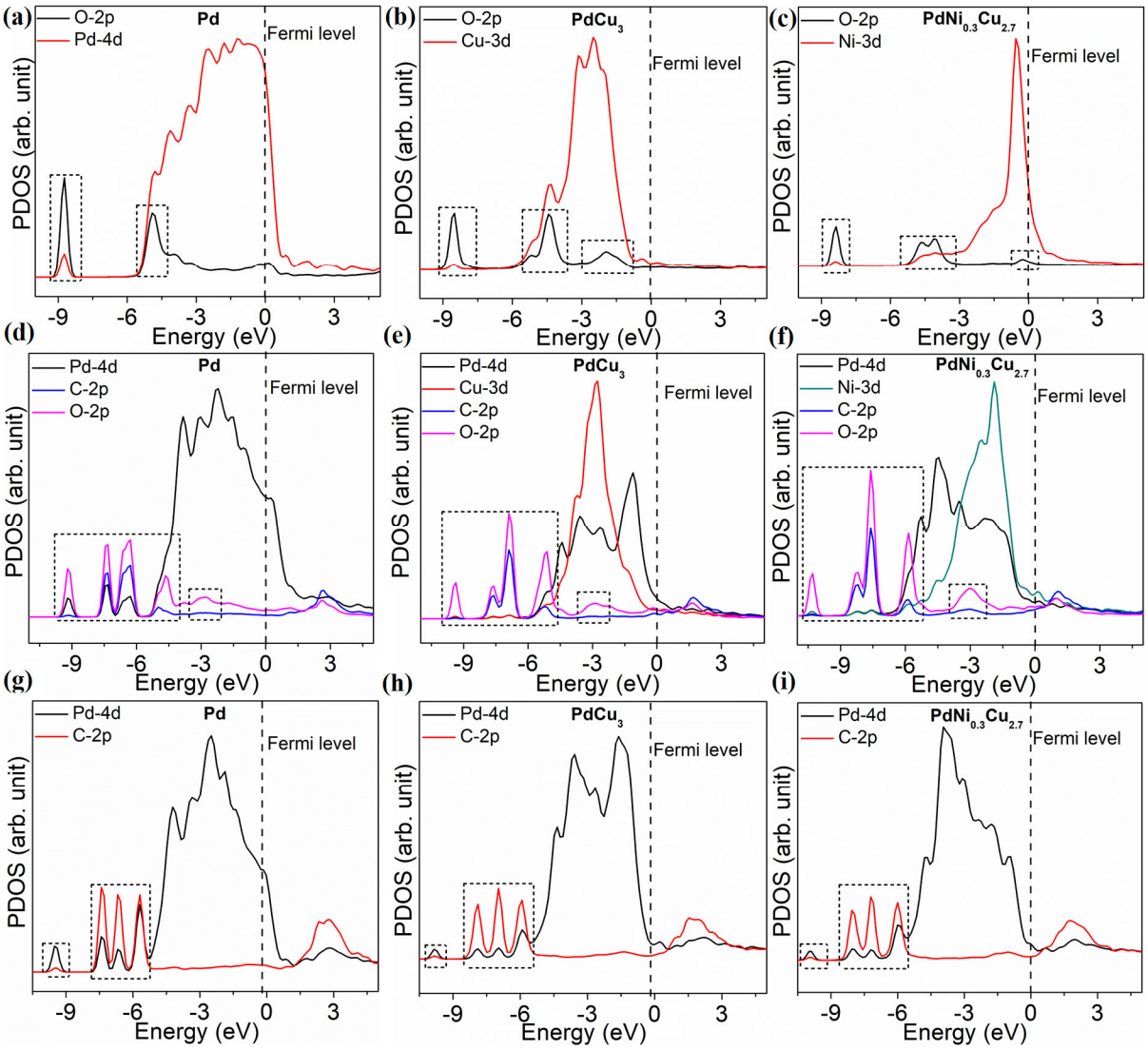

Fig. S23 Projected density of states (PDOS) plots for (a-c) OH adsorbed, (d-f) CH_3CO adsorbed, (g-i) CO adsorbed Pd, $PdCu_3$ and $PdNi_{0.3}Cu_{2.7}$ catalyst surfaces.

Projected density of states (PDOS) analysis further confirms the reverse adsorption behaviour of intermediates (Figure S23). The strong covalent bonding interactions (in the OH adsorbed surfaces) between *OH and M (M = Pd, Cu and Ni respectively) is evident from resonating O-2p and M-nd (n=3 and 4) orbitals. The relative position of this O-2p peaks determines the

relative strength of adsorption between adsorbates and catalyst surface. Peaks associated with O-2p orbitals gradually shift towards Fermi level from Pd to $PdCu_3$ and $PdNi_{0.3}Cu_{2.7}$ and it vividly confirms gradual strengthening of OH interaction with the corresponding surfaces. Conversely, resonating peaks of C-2p orbitals gradually shift deeper in energy (away from Fermi level) indicating relatively weaker adsorption of CO on $PdNi_{0.3}Cu_{2.7}$ compared to other surfaces. Similarly, interacting C-2p and O-2p orbitals of CH_3CO lies deeper in energy for CH_3CO adsorbed $PdNi_{0.3}Cu_{2.7}$ surface compared to other justifying the order of CH_3CO adsorption strength: $PdNi_{0.3}Cu_{2.7} < PdCu_3 <$ Pd.

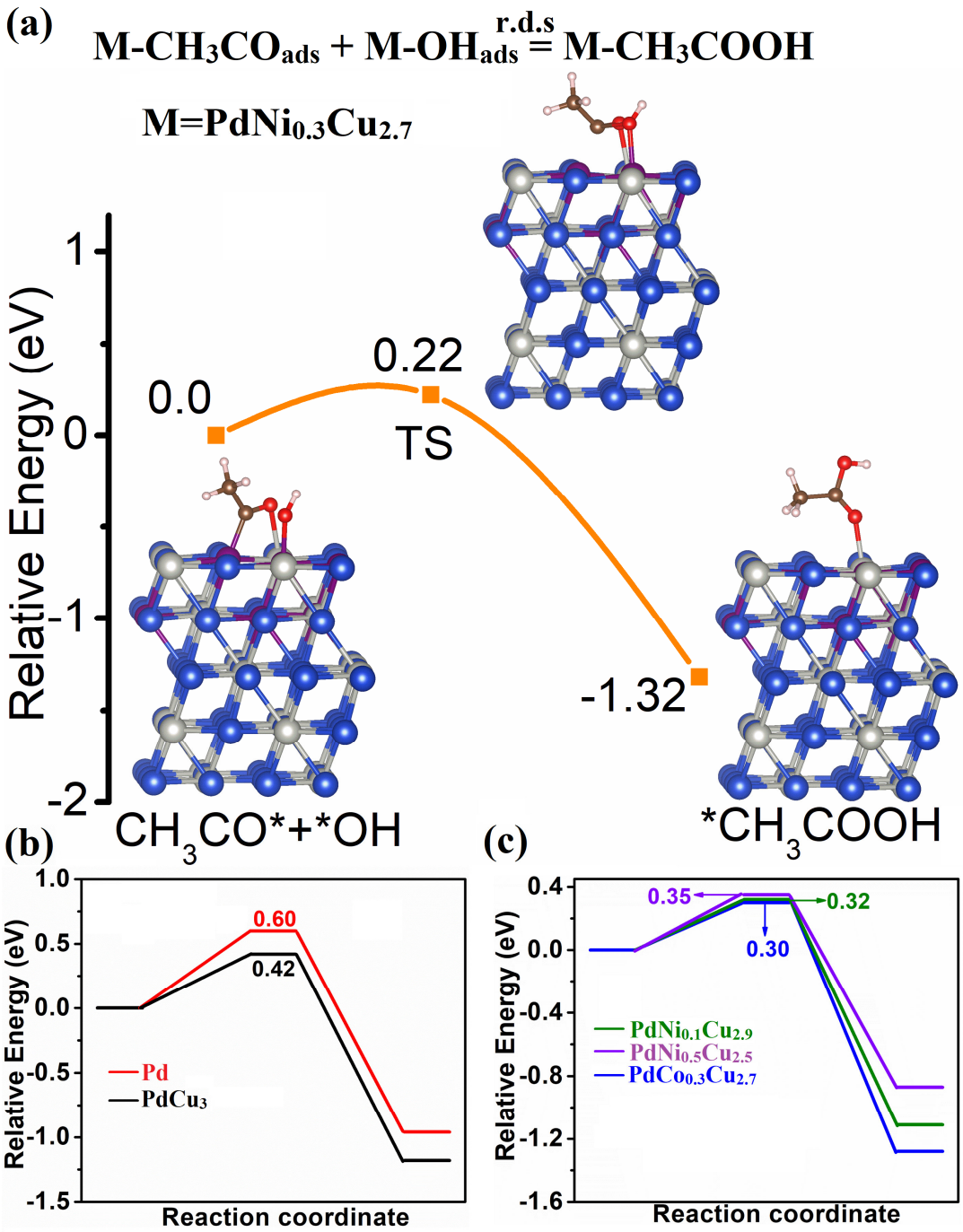

Fig. S24 Energy activation barriers ($\Delta E^{\ddagger}$) for the rate determining combination step (formation of CH_3COOH_{ads}) for different catalysts (111) surfaces.

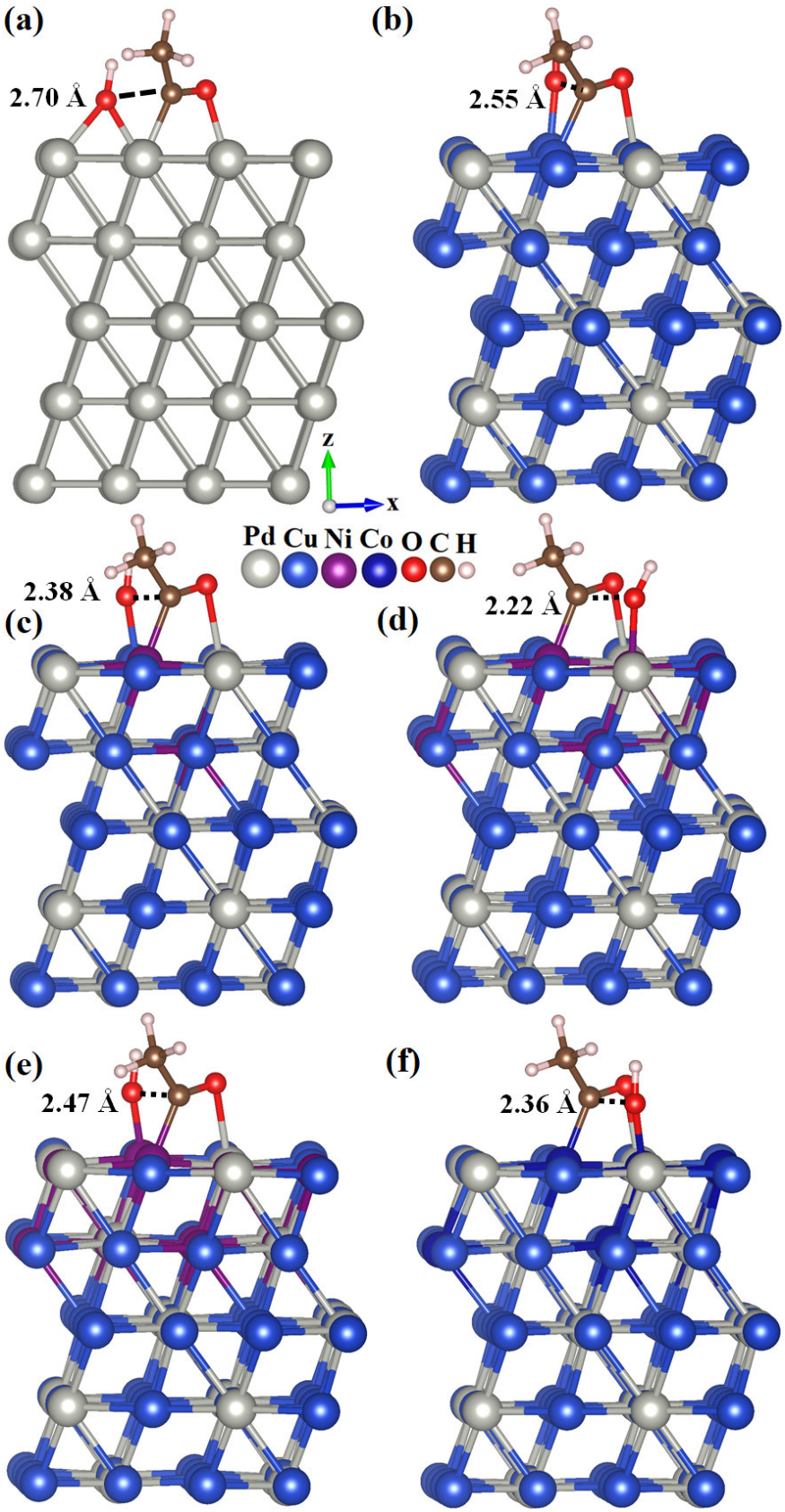

Fig. S25 Initial stage (IS) of the formation of adsorbed CH_3COOH on different catalyst surfaces (dotted line indicates the distance between C atom of CH_3CO_{ads} and O atom of OH_{ads}) (a) Pd, (b) ordered PdCu3, (c) $PdNi_{0.1}Cu_{2.9}$, (d) $PdNi_{0.3}Cu_{2.7}$, (e) $PdNi_{0.5}Cu_{2.5}$, (f) $PdCo_{0.3}Cu_{2.7}$.

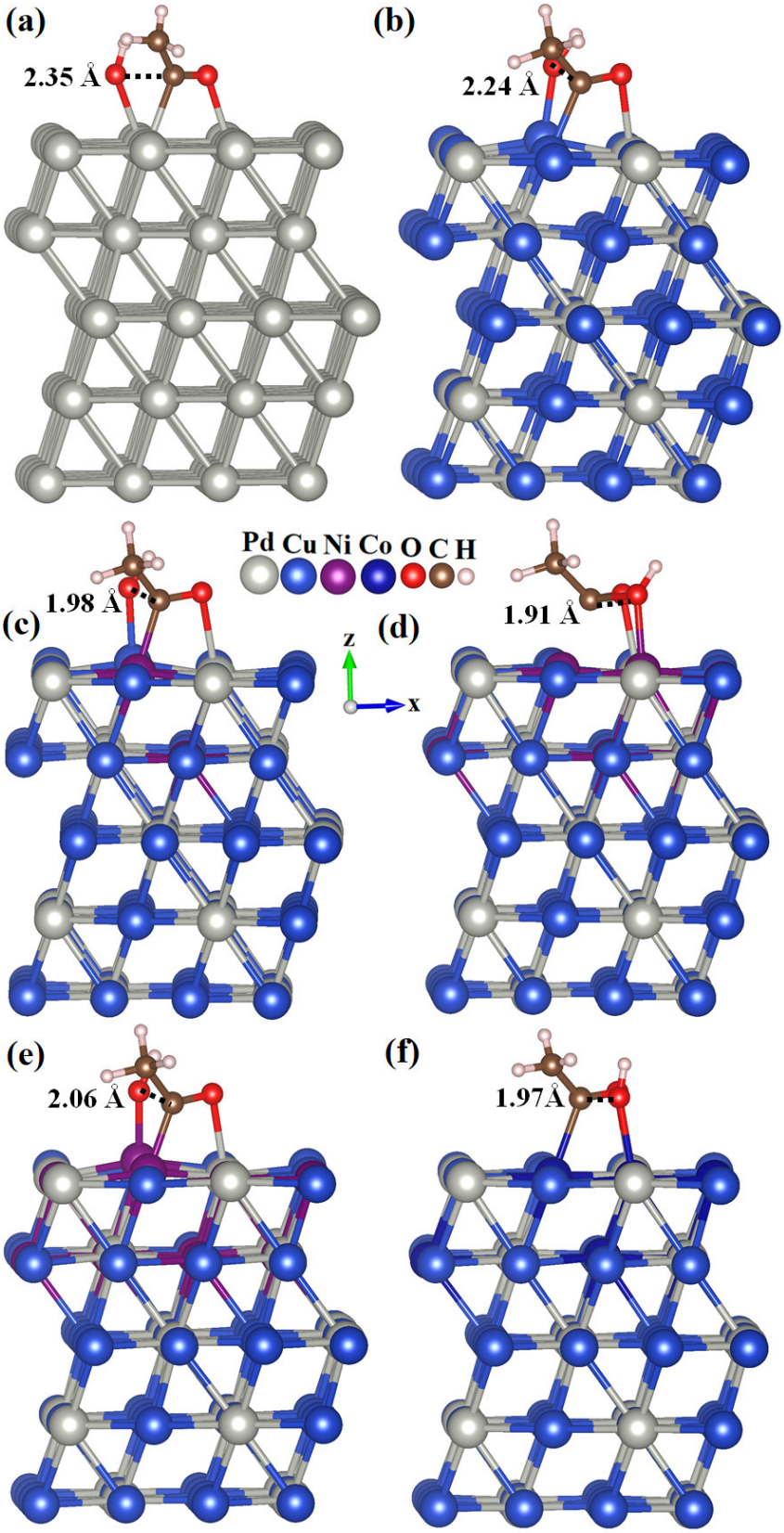

Fig. S26 Transition stage (TS) of the formation of CH_3COOH_{ads} on different catalyst (111) surfaces (dotted line indicates the distance between C atom of CH_3CO_{ads} and O atom of OH_{ads}) (a) Pd, (b) ordered $PdCu_3$, (c) $PdNi_{0.1}Cu_{2.9}$, (d) $PdNi_{0.3}Cu_{2.7}$, (e) $PdNi_{0.5}Cu_{2.5}$, (f) $PdCo_{0.3}Cu_{2.7}$.

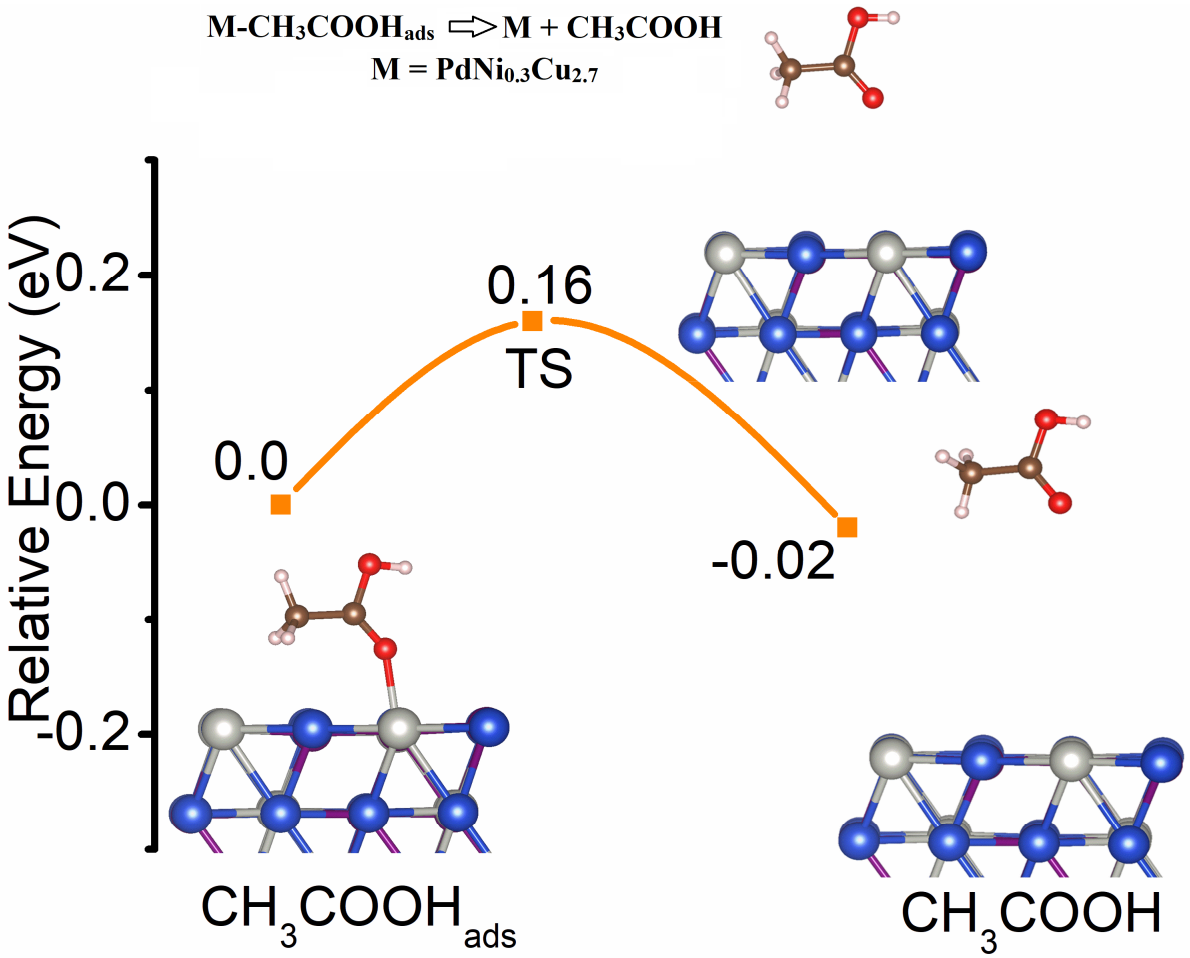

Fig. S27 Energy activation barriers (ΔE‡) for the desorption of CH3COOH from $PdNi_{0.3}Cu_{2.7}$ (111) surface.

Apart from the thermodynamic aspect, kinetics also play crucial role in catalysis. The energy activation barriers of the combination reaction (combination of $*CH_3CO$ and *OH) which is considered as rate limiting step for alkaline EOR, are calculated [using climbing image nudge elastic band method (CI-NEB)] to be 0.60, 0.42, 0.30 and 0.22 eV respectively for Pd, $PdCu_3$, $PdCo_{0.3}Cu_{2.7}$, $PdNi_{0.3}Cu_{2.7}$ (111) surfaces (Fig. 4f, S24 and Table S11). Relatively lower activation energy barrier (0.22 eV) compared to other catalysts confirms the faster EOR kinetics of $PdNi_{0.3}Cu_{2.7}$ catalyst. The lower activation energies of the substituted catalysts arises from the close proximity of the $*CH_3CO$ and *OH and it facilitates the formation of CH_3COOH (Fig. S25 and Table S12). The surface dependent preferential adsorption of OH radical in different catalysts occurs due to variation in the oxophilicity of the secondary transition metals (namely Co, Ni and Cu) leading to proximity difference of the key intermediates. Besides, a close look into the transition states (TS) of the combination step on various surfaces reveals the development of bonding interaction among the C atom of $*CH_3CO$ and O atom of *OH (Fig. S26 and Table S12). The distance between these two interacting atoms gradually decreases in TSs, thereby facilitating the combination step. The difference in EOR activity with the increase of Ni substitution is well understood in terms of intermediate adsorption and DBC. Besides, relatively higher activation barrier of $PdCo_{0.5}Cu_{2.5}$ (0.32 eV) compared to $PdCo_{0.3}Cu_{2.7}$ for CH_3COOH formation, makes EOR

kinetics sluggish and hence deteriorates the activity of $PdNi_{0.5}Cu_{2.5}$ compared to $PdNi_{0.3}Cu_{2.7}$. However, lower activation energy (c.a. 0.15 eV) of CH_3COOH desorption makes $PdNi_{0.3}Cu_{2.7}$ an ideal EOR catalyst (Fig. S27 and Table S11).

References

1. G. Kresse and J. Hafner, *Phys. Rev. B*, 1993, **47**, 558.
2. J. P. Perdew, K. Burke and M. Ernzerhof, *Phys. Rev. Lett.*, 1996, **77**, 3865.
3. R. Jana, C. Chowdhury, S. Malik and A. Datta, *ACS Appl. Energy Mater.*, 2019, **2**, 5613-5621.
4. R. Jana, C. Chowdhury and A. Datta, *ChemSusChem*, 2020, **13**, 3855-3864.
5. A. K. Mishra, A. Roldan and N. H. de Leeuw, *J. Phys. Chem. C*, 2016, **120**, 2198-2214.
6. S. Grimme, *J. Comput. Chem.*, 2006, **27**, 1787-1799.
7. M. Frisch, G. Trucks, H. Schlegel, G. Scuseria, M. Robb, J. Cheeseman, G. Scalmani, V. Barone, G. Petersson and H. Nakatsuji, *Journal*, 2016.
8. G. Henkelman and H. Jónsson, *J. Chem. Phys.*, 2000, **113**, 9978-9985.
9. R. Jana, A. Bhim, P. Bothra, S. K. Pati and S. C. Peter, *ChemSusChem*, 2016.
10. R. Yue, H. Wang, D. Bin, J. Xu, Y. Du, W. Lu and J. Guo, *Journal of Materials Chemistry A*, 2015, **3**, 1077-1088.
11. A.-L. Wang, H. Xu, J.-X. Feng, L.-X. Ding, Y.-X. Tong and G.-R. Li, *Journal of the American Chemical Society*, 2013, **135**, 10703-10709.
12. R. Jana, U. Subbarao and S. C. Peter, *Journal of Power Sources*, 2016, **301**, 160-169.
13. S. Sarkar, R. Jana, U. V. Waghmare, B. Kuppan, S. Sampath and S. C. Peter, *Chemistry of Materials*, 2015, **27**, 7459-7467.
14. H. Mao, T. Huang and A. Yu, *Electrochimica Acta*, 2015, **174**, 1-7.
15. M. Hasan, S. B. Newcomb, J. F. Rohan and K. M. Razeeb, *Journal of Power Sources*, 2012, **218**, 148-156.
16. F. Zhu, G. Ma, Z. Bai, R. Hang, B. Tang, Z. Zhang and X. Wang, *Journal of power sources*, 2013, **242**, 610-620.
17. C. Hu, X. Zhai, Y. Zhao, K. Bian, J. Zhang, L. Qu, H. Zhang and H. Luo, *Nanoscale*, 2014, **6**, 2768-2775.
18. W. Huang, X. Y. Ma, H. Wang, R. Feng, J. Zhou, P. N. Duchesne, P. Zhang, F. Chen, N. Han and F. Zhao, *Advanced Materials*, 2017, **29**, 1703057.
19. Y. Shu, Y. Zheng, Y. Ying, G. Yu, Y. Wu, Y. Wen and H. Yang, *Journal of The Electrochemical Society*, 2020, **167**, 064508.
20. A. R. Rajamani, P. Ashly, L. Dheer, S. C. Sarma, S. Sarkar, D. Bagchi, U. V. Waghmare and S. C. Peter, *ACS Applied Energy Materials*, 2019, **2**, 7132-7141.
21. Z. Yan, M. Zhang, J. Xie and P. K. Shen, *Journal of power sources*, 2013, **243**, 336-342.
22. W. Du, K. E. Mackenzie, D. F. Milano, N. A. Deskins, D. Su and X. Teng, *Acs Catalysis*, 2012, **2**, 287-297.
23. L. Chen, L. Lu, H. Zhu, Y. Chen, Y. Huang, Y. Li and L. Wang, *Nature communications*, 2017, **8**, 1-9.
24. X. Yu, Z. Luo, T. Zhang, P. Tang, J. Li, X. Wang, J. Llorca, J. Arbiol, J. Liu and A. Cabot, *Chemistry of Materials*, 2020, **32**, 2044-2052.
25. M. Yamauchi and T. Tsukuda, *Dalton Trans.*, 2011, **40**, 4842-4845.
26. A. Soutter, A. Colson and J. Hertz, *Mem. Etud. Sci. Rev. Metall*, 1971, **68**, 575-591.
27. M. Friedrich and M. Armbrüster, *Chem. Mater.*, 2009, **21**, 5886-5891.
28. D. M. Jones and E. Owen, *Proc. Phys. Soc., B*, 1954, **67**, 297.